(12)

CSDL-R-1982

SATELLITE AUTONOMOUS NAVIGATION WITH SHAD

by
R. L. White
R. B. Gounley

April 1987

The Charles Stark Draper Laboratory, Inc.
555 Technology Square
Cambridge, Massachusetts 02139

CSDL-R-1982

Final

SATELLITE AUTONOMOUS NAVIGATION WITH SHAD

by

R.L. White

R.B. Gounley

April 1987

The Charles Stark Draper Laboratory, Inc.

Cambridge, Massachusetts 02139

ACKNOWLEDGMENT

This report was prepared under Contract No. N00014-81-C-0803 and ARPA Order No. 4205 for the Office of Naval Research and the Defense Advanced Research Projects Agency. The research work under this contract was conducted during the period 1 September 1981 through 30 November 1982.

The authors wish to express their gratitude for the technical assistance and support provided by Eli Gai, Richard Battin, Frank Barnes, Milton Adams, and Mark Slutsky. The report was typed by Helen Conroy.

TABLE OF CONTENTS

SECTION 1

INTRODUCTION AND SUMMARY

1.1 Introduction

This report has been prepared as the Final Report of a preliminary study of the possible satellite autonomous navigation accuracy with the SHAD (Stellar Horizon Atmospheric Dispersion) concept for various types of representative orbits.

The SHAD concept is considered to be one of the most promising concepts yet identified for achieving high accuracy satellite autonomous navigation. Until now, the orbits of most satellites have been determined by using ground tracking measurements from radar systems, telescopes, etc. Unfortunately, earthbound tracking suffers from many limitations. Loss of a tracking station during wartime could prevent ground operators from obtaining the necessary orbit determination accuracy for certain military satellites. Ground tracking also limits civilian satellites since the high cost of tracking strains operating budgets and contributes to the cancellation of many otherwise cost-effective missions[1]. Furthermore, the large number of objects in orbit taxes the capacity of existing monitoring stations and delays their delivery of information to the operator[2].

In the near future, satellites will be able to navigate using signals from NAVSTAR satellites[3]. There are missions being planned, however, where even this degree of self-sufficiency may be inadequate[4].

To meet these needs, satellites can be built which estimate their positions without recourse to either ground stations or other satellites. Such an "autonomous navigation system" would allow a satellite to carry out many functions without instructions from the earth. Many people have suggested ways to navigate satellites autonomously; a few of these methods have already been implemented. However, the proposed and existing navigators have not been widely accepted, in part because of their inherent complexity, poor accuracy, or exorbitant computational requirements[5].

The SHAD concept takes advantage of the atmosphere's optical properties. Viewed from orbit, a star passing behind the earth's upper atmosphere will appear to be shifted upward from its true position. This refraction is a property of starlight frequency and atmospheric density. If a refraction measurement were to be made on a known star near the horizon, this would provide information on the direction of that portion of the earth's horizon with respect to the satellite in inertial coordinates. There are essentially two ways of measuring starlight refraction. One is is to measure the refraction directly such as with a star tracker. The other is to measure the difference in refraction (i.e. the dispersion) between two wavelengths of the starlight such as red and blue. The latter approach is utilized by the SHAD sensor and there are several advantages to performing the measurement in this manner. However, it should be noted that the above two methods are merely different ways of measuring the same basic phenomenon. The relationship between refraction and dispersion is very well known for air. Consequently, accurate measurements of one automatically imply accurate knowledge of the other.

Use of refraction or dispersion measurements for satellite navigation will require access to an accurate atmospheric refraction model and a star catalog. Each measurement will provide information about a particular component of satellite position. By performing these measurements on different stars throughout the orbit, a complete determination of the satellite position and velocity can be made. The accuracy of this determination will depend upon many paramenters such as measurement error, number and direction of star sightings, and type of satellite orbit. One of the primary objectives of this study is to provide some indication of the possible navigation accuracy and to indicate the sensitivity of performance to variation in the most important parameters.

1.2 Background

During the Apollo program, the Charles Stark Draper Laboratory (then the M.I.T. Instrumentation Laboratory) investigated many techniques for performing orbit navigation in the Command and Lunar Modules[6]. Early in this effort, mission planners felt that ground tracking was not sufficiently accurate or reliable enough to permit navigation of manned spacecraft over large distances. What was desired was a system that allowed the crew to determine its position without depending upon earth-based systems. Several navigation schemes considered for this purpose involved the sensing of the Earth's horizon either by measuring the horizon radiance in some portion of the electromagnetic spectrum (e.g. IR, UV, visible, etc.) or by measuring the effect on starlight (i.e. attenuation, refraction, etc.) when it grazes the atmosphere[7].

Although some of these approaches were very attractive, the technique finally adopted was to use a sextant-like device which measures the angle between an earth or lunar feature (e.g. landmark, limb, etc.) and a known star. By the time Apollo was launched, however, ground tracking had improved to the point where the autonomous navigation system could be relegated to back-up status.

In 1975, interest in horizon sensing by starlight refraction was renewed at CSDL in a Navy contract concerned with investigating all known techniques for autonomous navigation of vehicles traveling through space[8]. Though many people expressed doubts about accurately modeling and measuring starlight refraction, a few researchers felt that the method had potential since better star trackers were now available for this application and there was no indication that the refraction modeling was serious. Several sensor designs were conceived for accurately measuring starlight refraction; and a somewhat different type of sensor was jointly proposed by ONR, CSDL and Un. of MD in 1979 to measure the starlight dispersion instead of the refraction. Although dispersion is simply the variation in refraction with wavelength, previous development and tests of a two-color refractometer (TCR) at the Un. of MD indicated that this device could measure the dispersion between red and blue light with very high accuracy. For autonomous navigation, this device, with appropriate modifications for star acquisition, tracking, etc., is denoted as the SHAD sensor.

Having identified several ways of accurately measuring refraction or dispersion, there was still the problem of improving our knowledge of refraction modeling and the general behavior of the basic phenomenon. A

significant step was achieved in this direction when CSDL conducted a survey of existing satellites in late 1979 to determine if any could provide real data on stellar atmospheric refraction. Two NASA satellites (OAO-3 and HEAO-2) were found to have this capability and CSDL was granted guest observer status to obtain this data. Successful observations of refraction were obtained from OAO-3 (Orbiting Astronomical Observatory) on May 14 and July 11, 1980. Further experimentation with OAO-3 was not conducted since it was found that HEAO-2 (High Energy Astronomy Observatory) had inadvertently been making such observations with high accuracy since it was launched in November 1978. It is estimated that several thousand observations were made by HEAO-2 before it was deactivated in April 1981. Atleast 700 of these observations were retrieved and analyzed to some extent by CSDL, and a limited number of cases were processed with the highest available accuracy, using more accurate NASA determinations of the satellite orbit with ground tracking data. The results of that effort indicate that the concept has a very high navigation accuracy potential. The stratospheric density variations indicated by the more accurately processed data were much less than those indicated by meteorological balloon and rocket observations.

1.3 Summary

The primary objective of this study was to generate some indication of the autonomous navigation accuracy that can be achieved with the SHAD concept for various representative satellite orbits. This was accomplished by conducting a covariance analysis utilizing a Kalman filter to

sequentially process the measurements as they occur during orbit operation. Past experience has indicated that a significant amount of qualitative and reasonably accurate performance data can be conveniently generated with this type of simulation. Such data not only provides a fairly good indication of performance but also minimizes the number of cases that one may later wish to analyze more accurately with a full-state simulation utilizing elaborate gravity and atmospheric models, etc.

The performance results obtained in this investigation indicate that high-accuracy autonomous navigation is possible using relatively few stellar refraction/dispersion measurements per orbit. In the baseline cases examined, steady state position error standard deviations were often much less than 100 meters which is superior to most satellite navigation systems. Initial large uncertainties in the navigator's knowledge of satellite position and velocity were rapidly overcome within the first orbit of navigation and, thereafter, the performance slowly converged to steady-state levels in about five or six orbits.

Increasing the number of stars sighted per orbit improves overall accuracy but near-optimal performance can be achieved with relatively few sightings. Widening the azimuth span is valuable for optimizing accuracy in the normal direction. However, for a given number of visible stars in the sky, the best performance is obtained by making star sightings both fore and aft of the satellite's direction of motion.

The high accuracies obtained are, of course, due in large part to the low measurement variance used in the simulations. Preliminary refraction data from the satellite HEAO-2 show that the atmosphere is sufficiently stable in the tropics to warrant this low uncertainty. As more is learned about the upper atmosphere, this figure will certainly be revised to better

account for measurements taken all over the world. Furthermore, possible improvements in star sensor accuracy, not considered in this study, will also contribute significantly to the performance in high altitude satellites. Nevertheless, sensitivity studies on measurement standard deviations show that high accuracy navigation is possible even with less accurate measurements.

Simple models of the measurement bias show that we can obtain substantially better performance by accepting the biased measurements over the polar and temperate regions rather than excluding them. More sophisticated simulations, modeling bias over day and night regions as well as finer subdivisions of climatic zones, should be considered in future studies.

There is some indication, based on other independent navigation studies, that the process noise levels used in the present study are less than what they should have been for the relatively simple gravity modeling assumptions made for the navigator. If this is the case then the performance results in this report are somewhat optimistic for a simple navigator. However, they would be more correct for a navigator utilizing more complete models of gravity, drag, etc which is not only possible, but probably desirable.

As previously noted the present study was essentially a covariance analysis which provides a reasonably good indication of performance but does not provide the accuracy of a full-state simulation. When one considers the rather complex environment this concept must operate in, it would seem most appropriate to develop a full-state simulation in any future study of this concept.

SECTION 2

SATELLITE NAVIGATION BY STELLAR REFRACTION

2.1 Atmospheric Refraction

The passage of starlight through the earth's atmosphere bends the rays inward (see Figure 2-1). Viewed from orbit, the star's apparent position remains on the horizon long after it's true position has "set". In Figure 2-1 the refracted ray observed by the satellite appears to be grazing the earth at an apparent height h_a but actually grazes the earth at a slightly lower height denoted as h_g.

Refraction is strongest near the surface, becoming progressively weaker at higher altitudes. In effect, the atmosphere acts like a prism, refracting and dispersing the starlight passing through it. A ray of starlight passing through the spherical shell of the atmosphere encounters the gradient in air density which determines the amount by which the starlight is bent. Densities near the Earth's surface are known to be closely described by an exponential function of altitude such as the following:

$$\rho = \rho_o \exp\left(-\frac{h - h_o}{H}\right) \qquad (2\text{-}1)$$

where ρ is the density at altitude h, ρ_o is the density at some other altitude h_o, and H is the density scale height which is defined by

$$H = \frac{R_g T_m}{M_o g + R_g \left(\frac{dT_m}{dh}\right)} \qquad (2\text{-}2)$$

where R_g is the universal gas constant, T_m is the molecular scale temperature, M_o is the sea-level value of the molecular weight of air,

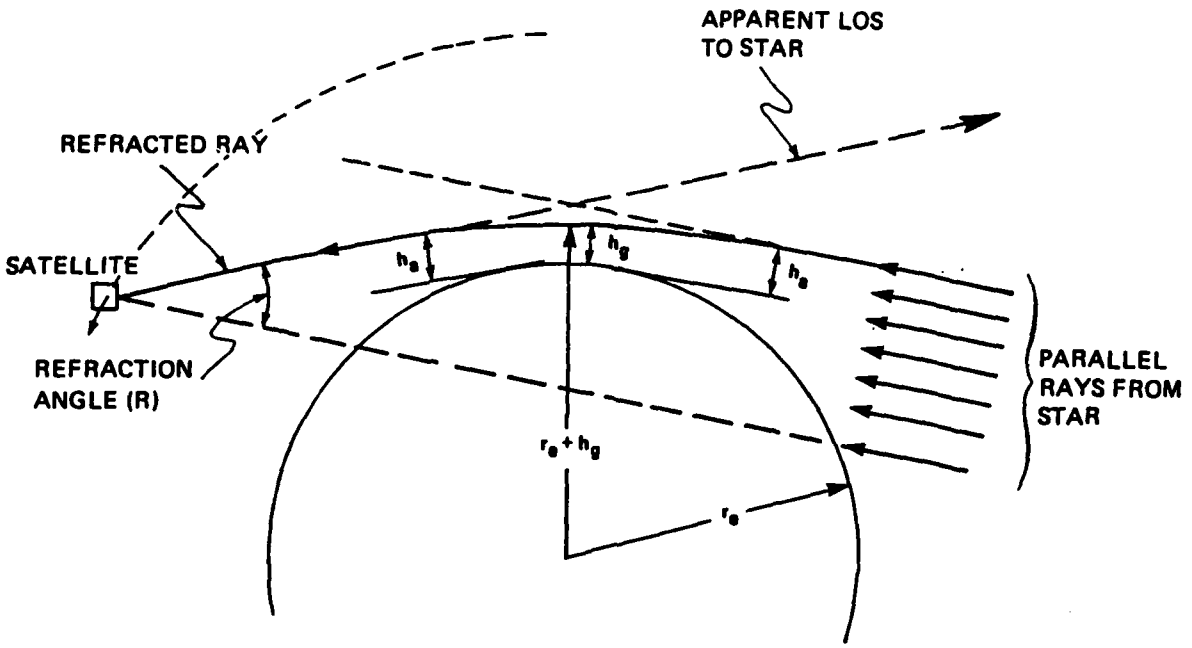

Figure 2-1. Starlight refraction

and g is the acceleration due to gravity. Another expression for the density scale height which may be easier to visualize is obtained by inverting Equation 2-1 to obtain:

$$H = (h-h_o)/\ \ln(\rho_o/\rho) \qquad (2\text{-}3)$$

Since the gravitational acceleration g and the molecular scale temperature T_m change with altitude for a realistic atmosphere, one can expect some change in H with altitude. However, the change in H over a limited altitude range is generally not very large.

If the value of H at some altitude h_g is assumed to be the same at all higher altitudes, an approximate value of the starlight refraction angle [7,8] is given as follows:

$$R \approx (\mu_g - 1)\left[\frac{2\pi\,(r_e + h_g)}{H_g}\right]^{\frac{1}{2}} \qquad (2\text{-}4)$$

where

R = total refraction (rad)

h_g = tangent (grazing) height of refracted ray (km)

r_e = earth radius (km)

μ_g = index of refraction at height h_g

H_g = density scale height at h_g (km)

According to Gladstone and Dale's law, the index of refraction (μ) is related to the air density (ρ) as follows:

$$\mu - 1 = k(\lambda)\rho \qquad (2\text{-}5)$$

where $k(\lambda)$ is denoted as the dispersion parameter and is a function of only the wavelength of the light. Therefore, the refraction angle in Equation 2-4 may be expressed in terms of the air density (ρ_g) at the grazing height (h_g) instead of the index of refraction (μ_g):

$$R \approx k(\lambda)\rho_g \left[\frac{2\pi\ (r_e + h_g)}{H_g}\right]^{\frac{1}{2}} \qquad (2\text{-}6)$$

where an expression for $k(\lambda)$ may be obtained by considering Equation 2-5 for air at standard temperature and pressure. According to Edlen[9] the index of refraction (μ_s) for air at standard temperature and pressure is related to light wavelength as follows:

$$(\mu_s - 1)\ 10^8 = 6432.8 + \frac{2949810}{146 - 1/\lambda^2} + \frac{25540}{41 - 1/\lambda^2} \qquad (2\text{-}7)$$

where λ is the wavelength in microns. The air density at standard temperature and pressure is 1225 g m^{-3}. Substituting the above values for air density and index of refraction into Equation 2-5 and solving for $k(\lambda)$ yields

$$k(\lambda) = 1 \times 10^{-8} \left(5.2513 + \frac{2408}{146 - 1/\lambda^2} + \frac{20.849}{41 - 1/\lambda^2}\right) \qquad (2\text{-}8)$$

To illustrate how well Equation 2-6 approximates the refraction of a realistic atmosphere such as the 1976 U.S. Standard Atmosphere,[10] the results with Equation 2-6 are compared in Table 2-1 with those generated by accurate ray tracing[11]. The refraction angle given by Equation 2-6 for

Table 2-1. Refraction angles for the 1976 U.S. Standard Atmosphere

Grazing Height (km)	Density Scale Height (km)	Refraction Angle (arcsec) Computed At λ = 0.7 microns By:	
		Equation 2-6	Accurate Ray Trace
20	6.225	331.7	333.8
25	6.366	147.9	148.1
30	6.519	67.2	67.3
35	6.508	30.9	30.7
40	6.897	14.2	14.1
45	7.288	6.8	6.7
50	8.047	3.4	3.3

each grazing height was computed using the density and density scale height indicated for that grazing height in the U.S. Standard Atmosphere. Note in Table 2-1 that the density scale height of the standard atmosphere does vary slightly.

2.2 Atmospheric Dispersion

Atmospheric dispersion represents the natural variation in atmospheric refraction with wavelength in accordance with the dispersion parameter $k(\lambda)$ given in Equation 2-8. The passage of starlight through the earth's atmosphere will cause the blue rays to bend more than the red rays (see Figure 2-2). A measure of the dispersion is provided by measuring the difference in refraction between the red and blue rays. Since the optical properties of natural air are well known, there is a well known relationship between dispersion and refraction for two wavelengths, and one may convert either type of measurement to its counterpart without significant loss of accuracy.

For a satellite at 1000 km altitude the values of dispersion observed between wavelengths of 0.35 and 0.7 microns for different grazing heights in the 1976 U.S. Standard Atmosphere are shown in Table 2-2[11]. Note that the dispersion values are small in comparison to the refraction values. However, it should be noted that a two-color refractometer has been developed which can very accurately measure the dispersion, and also has other design features of merit in the intended application. A detailed treatment of dispersion and its relationship to refraction is given in Section 2.4.6.

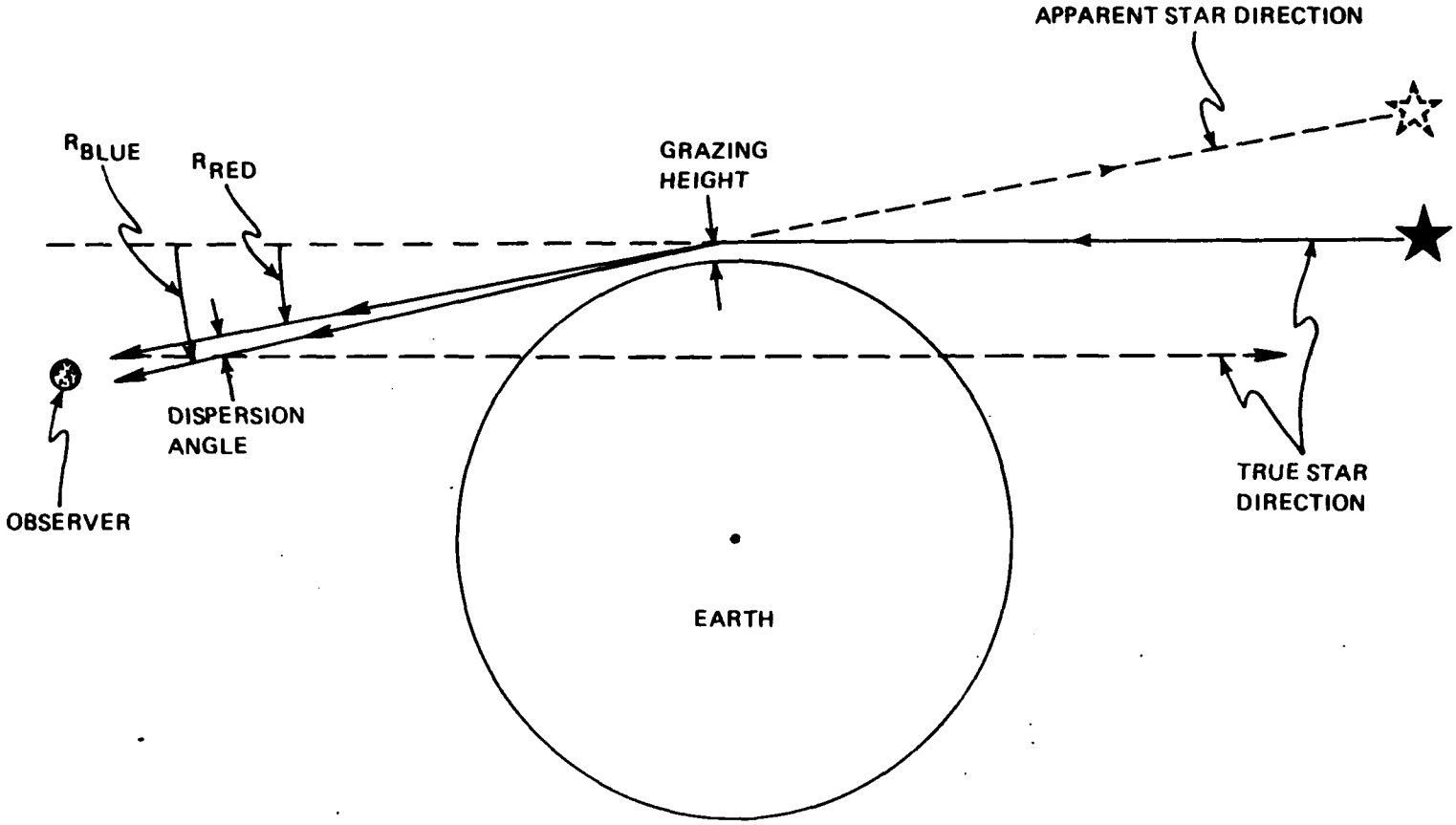

Figure 2-2. Starlight dispersion

Table 2-2. Approximate Values of Stellar Refraction and Dispersion at Wavelengths of 0.35 and 0.7 Microns for the 1976 U.S. Standard Atmosphere and a Satellite Altitude of 1000 Kilometers

Grazing Height (km)	Refraction at 0.7 microns (arcsec)	Dispersion Between 0.35 and 0.7 microns (arcsec)
20	333.76	6.44
25	148.13	3.88
30	67.27	2.12
35	30.69	1.05
40	14.07	0.50
45	6.70	0.25
50	3.34	0.12

2.3 Improved Atmospheric Density Models

The accuracy of horizon sensing with the SHAD concept will depend on our knowledge of the stratospheric density profile. Until now, most of the data on stratospheric density has been obtained indirectly through measurements of temperature and pressure made by instruments carried aloft in high-altitude balloons and rockets. Extensive temperature data has also been obtained with vertical sounders on satellites. The accuracy of the above measurements has generally been around 2 to 3 percent and, consequently, places a limit on how well the density can be estimated and modeled.

The variability of stratospheric density is known to be a function of at least latitude and season. Stratospheric observations with meteorological rockets and balloons indicate a density uncertainty at 25 km altitude of about 1.3 percent in the tropical region[12,13]. For the summer hemisphere the indicated density uncertainty may increase by a factor of two or three when going from the equator to the pole. However, the winter hemisphere, especially in the north, may experience local variations as high as 10 percent. It should be noted that most of the above data is based on temperature measurements which have been combined with pressure estimates to obtain density estimates. The errors in the density estimates for a given observation have generally been no better than one or two percent.

More accurate stratospheric density measurements on a worldwide basis would disclose certain systematic changes in the stratosphere, heretofore not known or firmly established because of limitations in existing data. Such an endeavor is being proposed as one of the objectives of a SHAD satellite experiment where either dispersion or refraction measurements

would be used in combination with very accurate independent knowledge of satellite position to estimate the observed density. Inspection of Equation 2-6 indicates that refraction is essentially a direct indication of density at the grazing altitude. Although the derivation of density from refraction measurements is not quite that straight-forward, relatively simple techniques have been developed and are now being used to estimate density from actual observations of refraction made by the satellite HEAO-2. Although this satellite was never designed to make stellar atmospheric refraction observations, CSDL discovered in late 1979 that HEAO-2 had inadvertently been making such observations with its two guide-star trackers since its launch date (November 1978), sometimes as often as once per orbit.

As of this writing, CSDL has processed about 700 HEAO-2 observations taken throughout the world between ± 45 degrees latitude. Detailed analysis of about 140 observations taken in the tropical region at different times of the year indicate that the stratospheric density variability is less than 1 percent. The accuracy of the HEAO-2 data in providing estimates of density is primarily limited by the accuracy of the HEAO-2 orbit determination from ground tracking data.

2.4 Navigation by Stellar Refraction or Dispersion

As noted previously, refraction and dispersion measurements may be regarded as merely two different, but closely related, ways of measuring the same basic refraction phenomenon. In the following subsections, a discussion is first given on how an observed refraction may be used for

satellite navigation. This is then followed by a discussion of dispersion and how it may be converted to an equivalent indication of refraction for the purposes of satellite navigation.

2.4.1 Basic Navigation Concept

Measurements of atmospheric refraction or dispersion for stars near the earth's horizon provide an indication of the direction of the horizon with respect to inertial space which, in turn, provides an indication of the satellite position with respect to an earth-centered inertial coordinate system. This is graphically illustrated in Figure 2-3 for the case where a satellite observes a particular value of refraction (e.g. 150 arcsec) for a known star. If one assumes a spherically symmetric atmosphere, all of the starlight refracted by a given amount will define a conical surface extending out into space and having an axis passing through the center of the earth in the direction of the star. Observation of this particular value of refraction by a satellite indicates that it is somewhere on the surface of the cone. By repeating the same type of observations on stars in different directions, the navigator can determine the satellite's complete position by essentially solving for the intersections of the various cones. It should be noted, however, that the complexity of solving for cone intersections is seldom necessary since the navigator usually has sufficiently accurate knowledge of the satellite position before each measurement to permit it to use a much simpler technique for position update. At the time of measurement, the navigator will usually have a prior estimate of the satellite position which will be in the vicinity of some small region of the cone. Since the measurement indicates that the

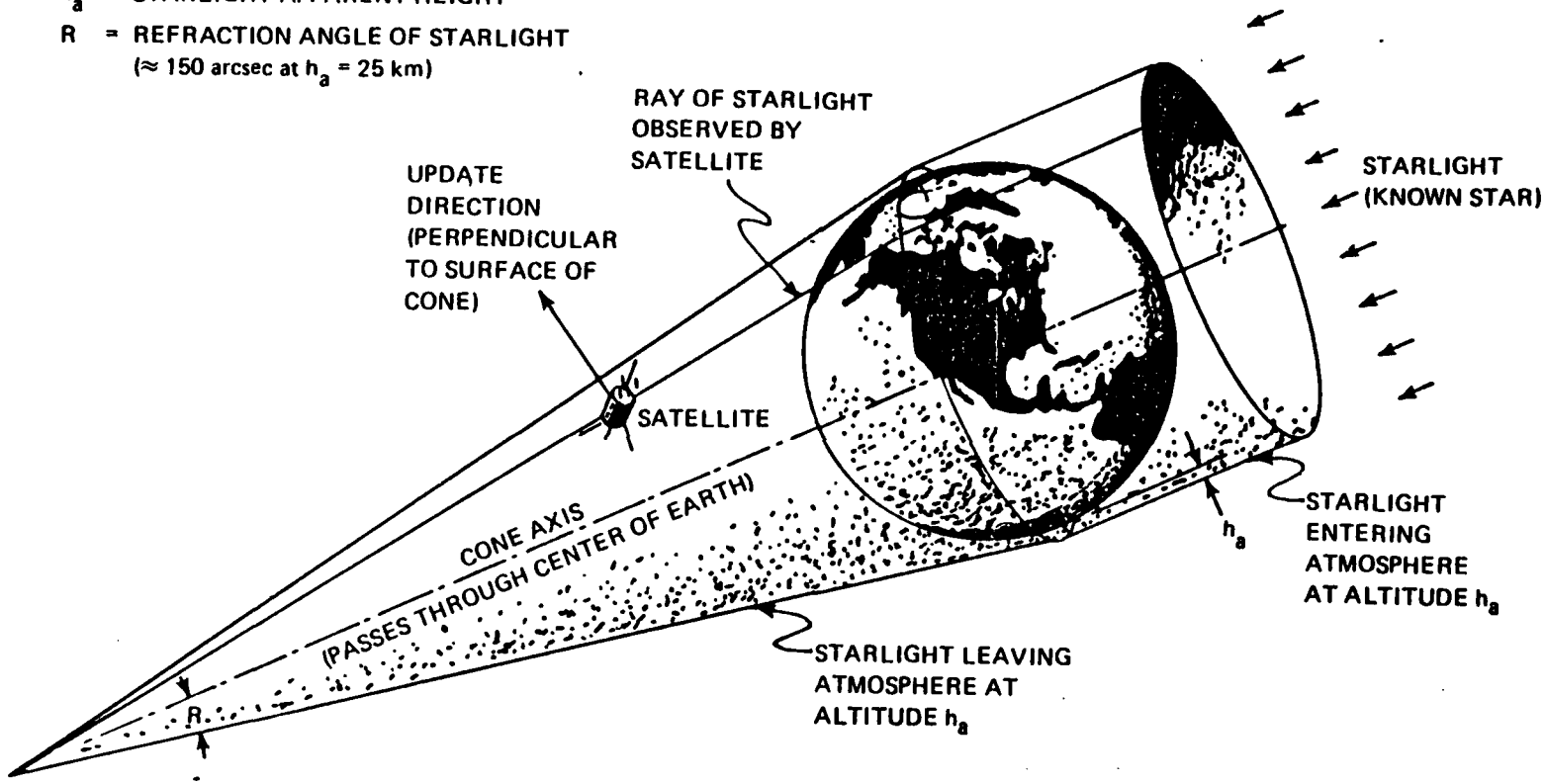

Figure 2-3. Autonomous navigation using measurements of starlight refraction

satellite is on the cone, the most probable position is that point on the cone closest to the estimated position. Thus, the navigator should update along the perpendicular from the estimated satellite position to the cone's surface.

It is apparent that the above update provides positional information in only one dimension. However, similar updates for horizon stars in other directions throughout the orbit will provide a complete update of position and velocity.

2.4.2 Refraction Cone Dimensions

The actual dimensions of the refraction cone are a function of the particular value of refraction being considered and the atmospheric density model assumed. For every star there is an infinite set of refraction cones corresponding to an infinite set of refraction angles and corresponding grazing altitudes. The apex angle of a given cone is equal to twice the refraction angle associated with that cone, while the base dimension is a function of the earth's diameter and the grazing height of the refracted light. The geometry associated with the base of the cone is shown in Figure 2-4. Here it is seen that the base radius might best be represented as a function of the apparent ray height (h_a) instead of the grazing ray height (h_g). For triangle AOB, the base radius (b) is:

$$b = (r_e + h_a)/\cos(R) \qquad (2\text{-}9)$$

Also note in Figure 2-4 that the base radius may be expressed as

$$b = r_e + h_a + a \qquad (2\text{-}10)$$

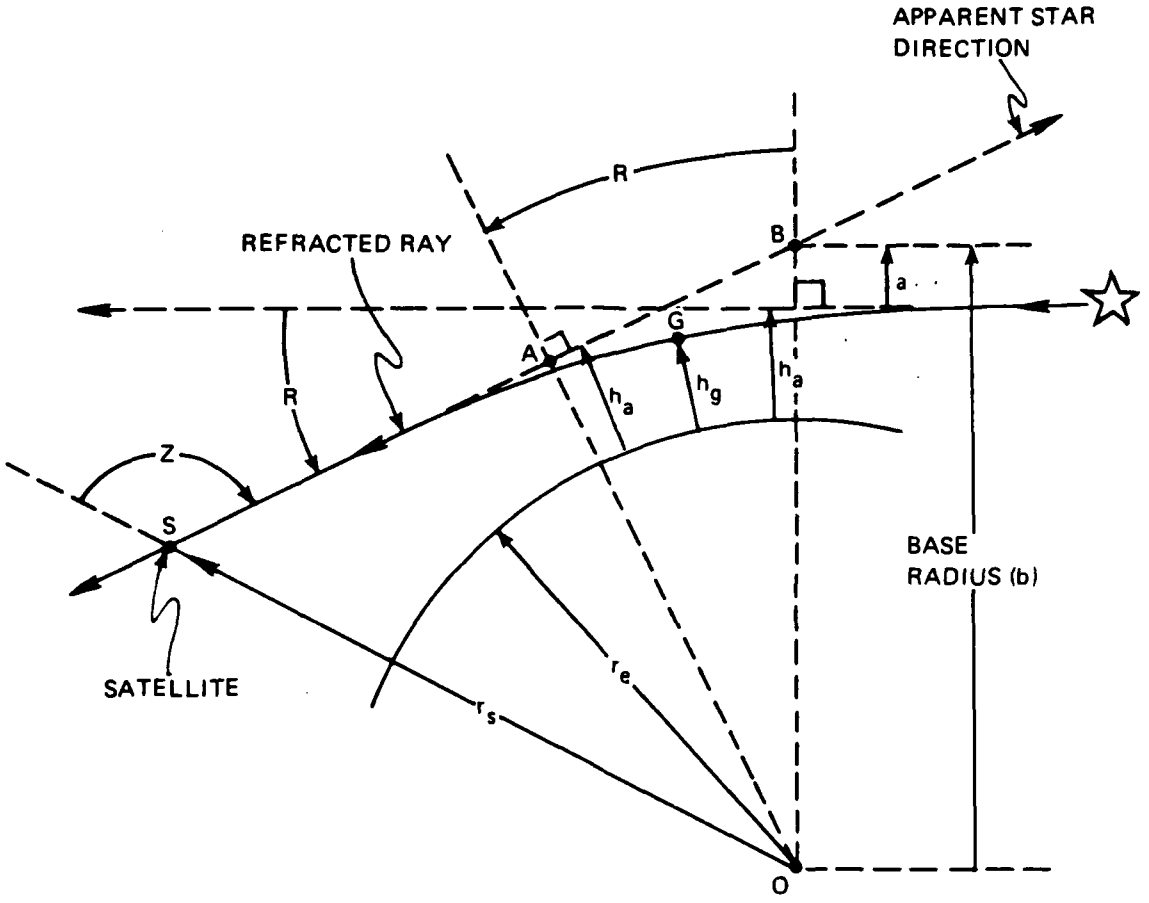

Figure 2-4. Cone base geometry

where the term (a) is a small distance which can be shown to be the following by equating Equation 2-9 to Equation 2-10:

$$a = \left(\frac{1}{\cos(R)} - 1 \right) \left(r_e + h_a \right)$$

For a typical refraction angle of 150 arc-seconds at h_a = 25 km, the term (a) will have a value of 1.69 meters which can usually be neglected so that

$$b \approx r_e + h_a \qquad (2\text{-}11)$$

It is important to note that the distance term (a) and the refraction (R) have been greatly enlarged in Figure 2-4 for ease of illustration. The refraction values of interest in this application are actually quite small and one could essentially visualize the refraction cone as being a cylinder.

Having expressed the radius of the cone's base as a simple function of h_a (Equation 2-11), there is the question of how h_a relates to h_g and the associated refraction for a given atmosphere.

If the atmosphere is spherically stratified in the region where refraction occurs, application of Snell's law leads to the following important relationship for any point on the ray path:

$$\mu \; r \sin(Z) = \text{Constant} \qquad (2\text{-}12)$$

where μ is the index of refraction at a given point, r is the radial distance of that point from the center of the earth, and Z is the zenith

angle of the ray at that point. The constant is sometimes referred to as the impact parameter and may be determined by applying Equation 2-12 to the grazing point G of Figure 2-4 where $Z = 90°$, $r = r_e + h_g$, and $\mu = \mu_g$, i.e.,

$$\text{Constant} = \mu_g \left(r_e + h_g\right) \tag{2-13}$$

Substituting the above value of the constant into Equation 2-12 and applying the equation to the satellite point S of Figure 2-4, where $Z = Z_s$ and $\mu = 1$, yields the following:

$$\sin(Z_s) = \mu_g \left(r_e + h_g\right) / r_s \tag{2-14}$$

Also note for triangle SAO of Figure 2-4 that

$$\sin(Z_s) = \left(r_e + h_a\right) / r_s \tag{2-15}$$

Therefore

$$r_e + h_a = \mu_g \left(r_e + h_g\right) \tag{2-16}$$

or

$$h_a = r_e \left(\mu_g - 1\right) + \mu_g h_g \tag{2-17}$$

Note that the above relationship between h_a and h_g requires only the index of refraction at h_g. Also, note that this relatively simple relationship applies to any spherically stratified atmosphere, whether it varies exponentially with altitude or otherwise. Since μ_g can be expressed in terms of ρ_g and $k(\lambda)$ in accordance with Gladstone and Dale's law, Equation 2-17 may also be expressed as follows:

$$h_a = k(\lambda)\, \rho_g (r_e + h_g) + h_g \qquad (2\text{-}18)$$

At the altitudes of interest in the present study (i.e. 20 km and greater), the first term on the right of Equation 2-18 will be very small, causing h_a to be slightly larger than h_g. An indication of the relative magnitudes of h_a and h_g is given in Table 2-3 for two different representative atmospheres (1976 U.S. Standard and 1962 Tropical). Note that the values of h_a obtained with Equation 2-18 are the same as those obtained by accurate ray tracing. This is to be expected since the ray-trace results were for two atmospheres which were assumed to be spherically stratified. Also note that the relationship between h_a and h_g is essentially the same for both of the atmospheres considered in Table 2-3, even though there are larger proportional differences in the corresponding densities and refraction angles. At a grazing height of 20 km it is seen that the density is about 7 percent higher for the tropical atmosphere. However, the corresponding apparent height is only 9 meters higher.

2.4.3 Relationship Between Satellite Position and Refraction Cone

Having established the dimensions of the refraction cone as a function of refraction angle and apparent ray height, the question is now one of how a refraction measurement can be used to relate the satellite position to the cone. This problem is facilitated by introducing a new quantity referred to as the vacuum tangent height (h_v) of the star LOS (i.e. the tangent height of the star LOS if no atmosphere were present). It will be shown that the vacuum tangent height provides the "connecting link" between the satellite position and the refraction cone since it may be expressed

Table 2-3. Refraction data at λ = 0.7 microns for the 1976 U.S. Standard and 1962 Tropical Atmospheres

h_g (km)	h_a (km) Estimated By		Density (ρ_g) (g/m^3)	R (arcsec)
	Equation 2-18	Ray Tracing		
U.S. Standard:				
20	20.128	20.128	88.910	333.76
25	25.058	25.058	40.084	148.13
30	30.027	30.027	18.410	67.27
35	35.012	35.012	8.463	30.70
40	40.006	40.006	3.996	14.07
Tropical:				
20	20.137	20.137	95.154	376.49
25	25.058	25.058	40.450	150.46
30	30.026	30.026	18.306	66.27
35	35.012	35.012	8.600	30.37
40	40.006	40.006	4.181	14.47

either as a function of star direction and satellite position only or approximately as a function of refraction and one particular component of satellite position with very little error.

Figure 2-5 illustrates how h_v is related to star direction and satellite position. The satellite position vector ($\underline{r}$) can be expressed as the sum of two orthogonal vector components as follows:

$$\underline{r} = (\underline{r} \cdot \underline{u}_s)\, \underline{u}_s + (\underline{r} \cdot \underline{u}_{up})\, \underline{u}_{up} \qquad (2\text{-}19)$$

where $\underline{u}_s$ is a unit vector in the known star direction and $\underline{u}_{up}$ is a unit vector normal to $\underline{u}_s$ and in the plane defined by $\underline{u}_s$ and $\underline{r}$, i.e.

$$\underline{u}_{up} = \text{Unit}\left[\underline{u}_s \times (\underline{r} \times \underline{u}_s)\right] \qquad (2\text{-}20)$$

Note in Figure 2-5 that h_v can be expressed in terms of the magnitude of the second vector component of $\underline{r}$ of Equation 2-19 as follows:

$$h_v = \underline{r} \cdot \underline{u}_{up} - r_e \qquad (2\text{-}21)$$

Equation 2-21 therefore gives the relationship between h_v and satellite position without any consideration being made for refraction.

Figure 2-6 illustrates how h_v may also be expressed in terms of the refraction angle (R), the apparent ray height (h_a), and the magnitude of the other orthogonal component of satellite position. Using triangle BSE, the vacuum tangent height can be expressed as follows:

$$h_v = h_a + a - d \tan(R) \qquad (2\text{-}22)$$

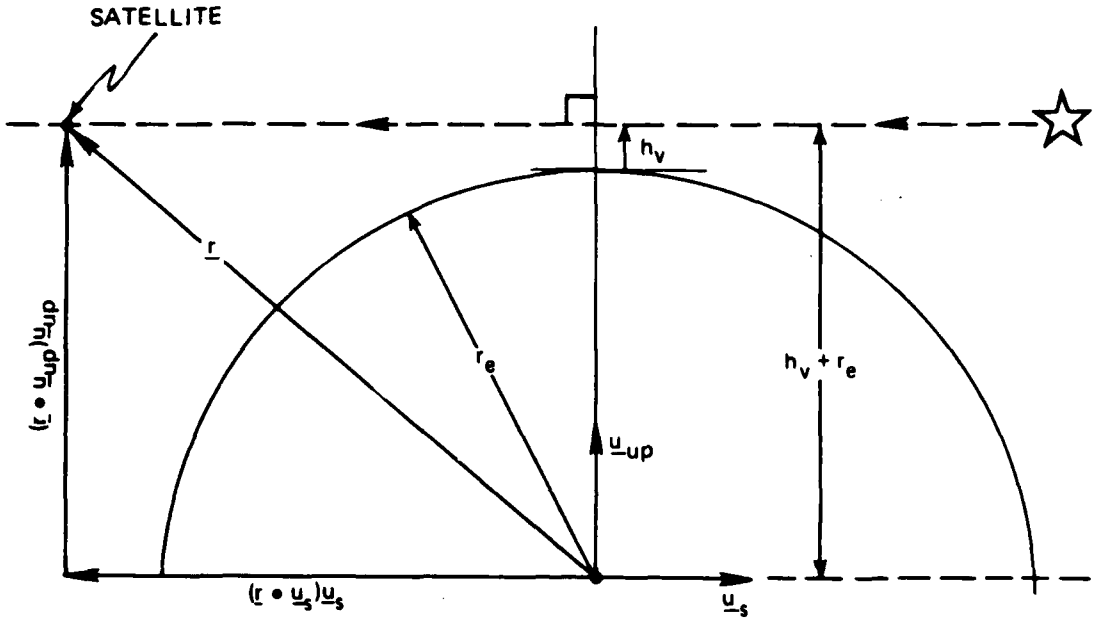

Figure 2-5. Relationship between h_v and satellite position

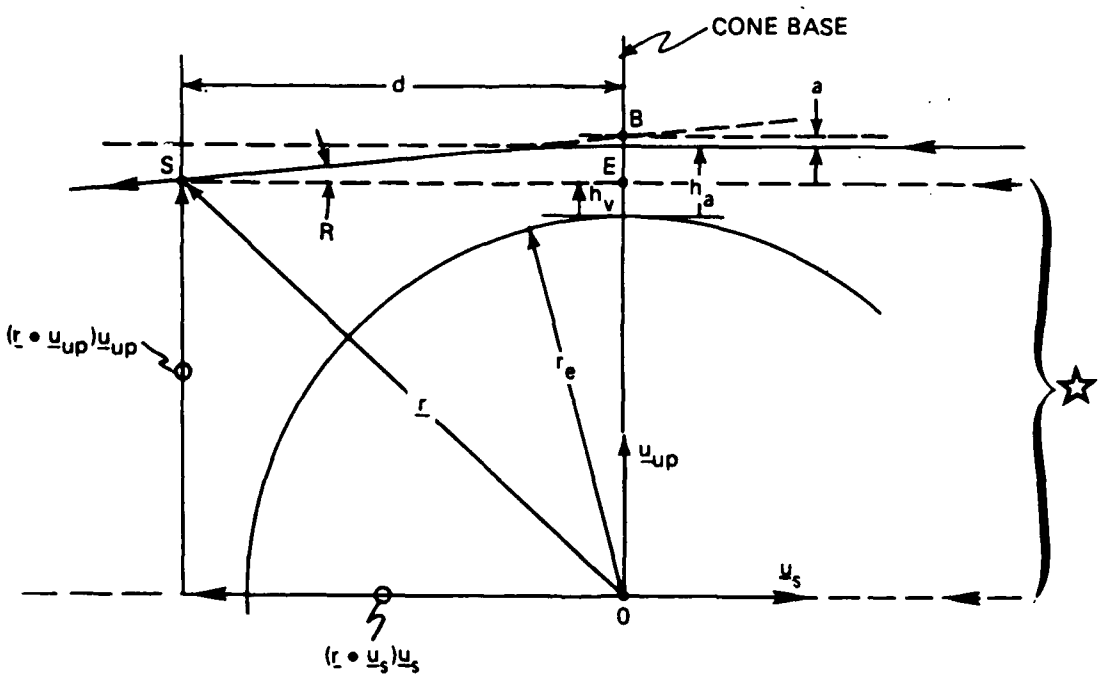

Figure 2-6. Relationship between h_v and refraction angle R

where d is the distance of the satellite from the cone base and a is the small distance previously indicated to be negligible. Note that d is equal to the magnitude of $(\underline{r} \cdot \underline{u}_s)$ so that Equation 2-22 may be expressed as follows:

$$h_v = h_a + a - \left|\underline{r} \cdot \underline{u}_s\right| \tan(R) \qquad (2\text{-}23)$$

Equation 2-23 therefore gives the relationship between h_v and the refraction cone. In addition, this equation may also be regarded as the measurement equation for satellite navigation since its relates h_v to the measured refraction and the apparent height which may be derived from the measured refraction for a known atmospheric density profile. The relationship between refraction and apparent height is independent of satellite position and may be represented by the following general expression which expresses h_a as a function of R and the atmospheric density profile (denoted merely as ρ):

$$h_a = h_a(R, \rho) \qquad (2\text{-}24)$$

Since the atmospheric density profile is assumed to be known in the case of satellite navigation, the apparent height for a given refraction can be obtained analytically or by interpolating a table of precomputed matching values of h_a and R. In the case of an exponential atmosphere, the density profile is exponential by definition and an approximate analytical expression of h_a (see Appendix A) is as follows:

$$h_a(R, \rho_o) = h_o - H \ln(R) + H \ln\left\{k(\lambda)\, \rho_o \left[\frac{2\pi\, r_e}{H}\right]^{\frac{1}{2}}\right\} + R\left[\frac{H\, r_e}{2\pi}\right]^{\frac{1}{2}} \qquad (2\text{-}25)$$

where ρ_o is the density at some arbitrary reference height h_o, and H is the fixed density scale height. This expression will be used later to indicate the effect on h_v of errors in R and ρ. For the moment, however, the function in Equation 2-24 is assumed to be that for any known arbitrary atmosphere, and when substituted for h_a in Equation 2-23 yields the following:

$$h_v = h_a(R, \rho) + a - \left|\underline{r} \cdot \underline{u}_s\right| \tan(R) \qquad (2\text{-}26)$$

This expression for h_v provides the key for how a refraction measurement may be used to update satellite position. As previously shown in Equation 2-19, the satellite position vector can be expressed as the sum of two orthogonal vector components as follows:

$$\underline{r} = (\underline{r} \cdot \underline{u}_s)\, \underline{u}_s + (\underline{r} \cdot \underline{u}_{up})\, \underline{u}_{up} \qquad (2\text{-}27)$$

where $\underline{u}_s$ is the unit star vector and $\underline{u}_{up}$ is a unit vector normal to $\underline{u}_s$ and in the plane defined by $\underline{u}_s$ and $\underline{r}$. Although $\underline{u}_{up}$ is normal to the star direction, and not the cone's surface, the difference in direction is negligible since the refraction angles are small. From Equation 2-21 the magnitude of the second vector component of Equation 2-27 can be expressed as follows:

$$\underline{r} \cdot \underline{u}_{up} = h_v + r_e \qquad (2\text{-}28)$$

Substituting the expression for h_v from Equation 2-26, neglecting the small distance a, and assuming $R \approx \tan(R)$, yields:

$$\underline{r} \cdot \underline{u}_{up} = h_a(R,\rho) - \left|\underline{r} \cdot \underline{u}_s\right| R + r_e \qquad (2\text{-}29)$$

which when substituted into Equation 2-27 yields the final expression relating the satellite position vector to the refraction angle and atmospheric density:

$$\underline{r} = (\underline{r} \cdot \underline{u}_s)\, \underline{u}_s + \left[h_a(R,\rho) - \left| \underline{r} \cdot \underline{u}_s \right| R + r_e \right] \underline{u}_{up} \qquad (2\text{-}30)$$

Here it is seen that only the position component in the direction of $\underline{u}_{up}$ would be updated by a refraction measurement.

2.4.4 Error Relationships Between Satellite Position, Refraction Angle and Atmospheric Density

A good indication of the effect of errors in refraction measurement and atmospheric density modeling on satellite position update can be obtained by considering the case of an exponential atmosphere which agrees with the 1976 U.S. Standard Atmosphere at 25 kilometers altitude. Substituting the expression for $h_a(R,\rho)$ from Equation 2-25 into Equation 2-29 and differentiating gives:

$$d(\underline{r} \cdot \underline{u}_{up}) = H \frac{d\rho_o}{\rho_o} - H \frac{dR}{R} - \left| \underline{r} \cdot \underline{u}_s \right| dR + \left[\frac{H\, r_e}{2} \right]^{\frac{1}{2}} dR \qquad (2\text{-}31)$$

where $\left| \underline{r} \cdot \underline{u}_s \right|$ is the distance of the satellite from the cone base which may be approximated as:

$$\left| \underline{r} \cdot \underline{u}_s \right| \approx \left(r_s^{\,2} - (6400)^2 \right)^{\frac{1}{2}} \qquad (2\text{-}32)$$

Inspection of Equation 2-31 indicates a relatively simple relationship between the satellite position error $\left(d(\underline{r}\cdot\underline{u}_{up})\right)$, refraction measurement error (dR), and density error ($d\rho_o$). Note that the first two error terms on the right of Equation 2-31 are proportional to the percentage error in density or refraction; the third term is proportional to the refraction error and the distance to the cone base; and the last term, which happens to be very small, is proportional to only the refraction error.

At 25 kilometers altitude, Tables 2-1 and 2-3 give the following values for the U.S. Standard Atmosphere:

$$H = 6.366 \text{ km}$$

$$\rho_o = 40.084 \text{ gm/m}^3$$

$$R = 148.1 \text{ arc second } (0.000718 \text{ rad})$$

For a one percent error in our knowledge of density at 25 kilometers, Equation 2-31 indicates that this will cause a satellite position error of 63.7 meters. Likewise, a one percent error (1.48 arc seconds) in refraction measurement for a satellite at an altitude of 1000 kilometers will cause an overall satellite position error of 89.4 meters (i.e., 63.7 meters for the percentage error term and 25.7 meters for the last two terms of Equation 2-31).

2.4.5 Adoption of h_v as Navigation Measurement

It is interesting to note that the satellite position error given by Equation 2-31 can also be interpreted as an equivalent error in the indicated vacuum tangent height since

$$h_v = \underline{r} \cdot \underline{u}_{up} - r_e \qquad \text{(from Equation 2-28)}$$

$$dh_v = d\left(\underline{r} \cdot \underline{u}_{up}\right) \qquad \text{(assuming } dr_e = 0\text{)}$$

Therefore

$$dh_v = H \frac{d\rho_o}{\rho_o} - H \frac{dR}{R} - \left|\underline{r} \cdot \underline{u}_s\right| dR + \left[\frac{H\, r_e}{2\,\pi}\right]^{\frac{1}{2}} dR \qquad (2\text{-}33)$$

For the purposes of the present study, Equation 2-33 suggests that it would be simpler to consider h_v, rather than R, as the parameter being measured since it conveniently includes the error-effects of density and refraction measurement, and permits one to express the overall error in common units of meters. This approach was taken in the present study and very little comment is made in the later sections of this report about the relative contributions of each error source since this is considered to be somewhat arbitrary in a general study of this type. Most of the navigation performance data generated in the current study was for a baseline measurement error of 70 meters in h_v, although some data was generated for other values. An indication of the error in h_v for various values of refraction measurement error combined with a one percent error in density is provided in Table 2-4 for three different satellite altitudes. The results were generated using Equation 2-33. Assuming a density error of one percent, it is seen that the baseline value of 70 meters adopted for the current study is representative of what one could expect with a refraction measurement error of 0.5 arc second at a satellite altitude of 1000 kilometers, or with a refraction measurement error of 0.1 arc second at geostationary altitude. It should be noted that the star trackers on the satellite HEAO-2 demonstrated a refraction measurement accuracy of better than 0.5 arc second.

Table 2-4. Equivalent h_v Error for Various Refraction Measurement Errors Combined with a One Percent Density Error. (For Observation at 25 km Grazing Altitude)

Satellite Altitude (km)	Density Error (%)	Refraction Error (arcsec)	Equivalent h_v Error (m) For		RSS
			ρ_o	R	(m)
1000	1	1.0	64	60	88
		.5		30	71
		.1		6	64
20,242 (GPS)		1.0		168	180
		.5		84	106
		.1		17	66
35,866 (Geo)		1.0		276	283
		.5		138	152
		.1		28	70

2.4.6 Navigation with Dispersion Measurements

The dispersion represents the difference in refraction between two wavelengths of light. According to Equation 2-6 the refraction at wavelength λ for an exponential atmosphere is approximately

$$R(\lambda) \approx k(\lambda)\, \rho_g \left(2\pi b\, (r_e + h_g) \right)^{\frac{1}{2}} \qquad (2\text{-}34)$$

where ρ_g is the density at grazing height h_g, and b is the inverse density scale height (i.e. $b = 1/H$). Since $h_g << r_e$, the refraction may be expressed fairly accurately as

$$R(\lambda) \approx k(\lambda)\, \rho_g \left(2\pi b\, r_e \right)^{\frac{1}{2}} \qquad (2\text{-}35)$$

Using subscripts b and r to denote the blue and red wavelengths, and denoting ρ_b and ρ_r as the densities at the grazing heights for the blue and red rays, the dispersion between the two rays is

$$\delta = R_b - R_r$$

$$\delta = \left(2\pi b\, r_e \right)^{\frac{1}{2}} \left(k_b\, \rho_b - k_r\, \rho_r \right)$$

Since

$$\rho_b = \rho_r\, e^{-b \left(h_{g_b} - h_{g_r} \right)} \qquad (2\text{-}36)$$

$$\delta = k_r \rho_r \left(2\pi b \, r_e \right)^{\frac{1}{2}} \left[\frac{k_b}{k_r} e^{-b\left(h_{g_b} - h_{g_r}\right)} - 1 \right]$$

$$\delta = R_r \left[K e^{-b\left(h_{g_b} - h_{g_r}\right)} - 1 \right] \qquad (2\text{-}37)$$

where $K = k_b/k_r$.

A particular value of δ sometimes useful in the present instance is that value commonly referred to as the local dispersion angle (δ_ℓ). This is the dispersion between the red and blue rays for the same grazing height where

$$\delta_\ell = R_r(K-1) \qquad (2\text{-}38)$$

It is important to note, however, that a satellite cannot observe δ_ℓ since the red and blue rays for the same grazing height will diverge after passing through the atmosphere and are sufficiently separated by the time they reach a satellite that they cannot be observed simultaneously with reasonable size optics. Likewise, a satellite cannot observe the dispersion given by Equation 2-37 except for the case where the red and blue rays converge to a point at the satellite as shown in Figure 2-7. Note in Figure 2-7 that the grazing height of the blue ray must be above that of the red ray since the refraction is larger for the blue ray.

To guarantee that a satellite can observe the dispersion given in Equation 2-37, a constraint must be placed on the difference in ray grazing heights shown in that equation. This constraint will be a function of the

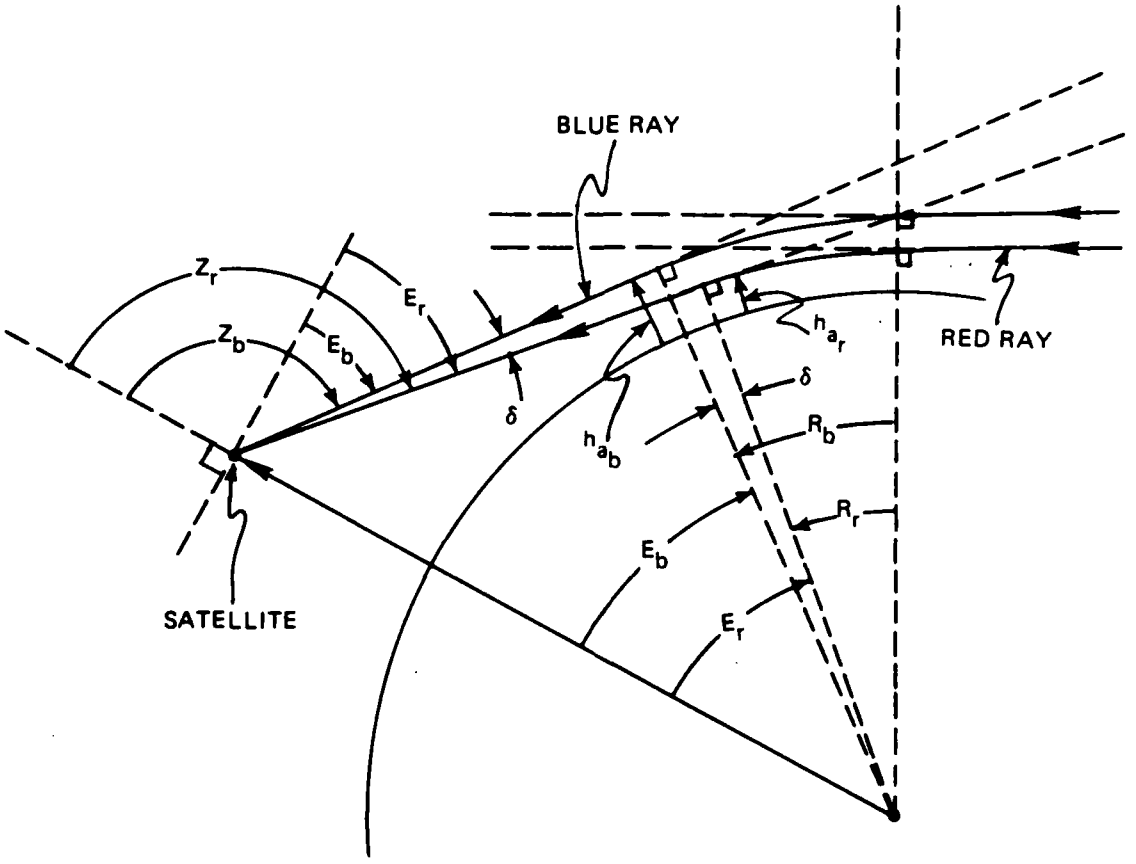

Figure 2-7. Dispersion geometry

satellite distance from the horizon. In the following derivation, the required difference in grazing heights is determined by first expressing the grazing height difference in terms of the corresponding difference in apparent heights. Afterwards, the desired constraint is placed on the apparent heights so that ray convergence occurs at the satellite:

According to Equation 2-18 the grazing height difference can be expressed in terms of the apparent height difference as follows:

$$h_{g_b} - h_{g_r} = \frac{h_{a_b} - k_b \rho_b r_e}{1 + k_b \rho_b} - \frac{h_{a_r} - k_r \rho_r r_e}{1 + k_r \rho_r}$$

Since the denominator terms $k_b \rho_b$ and $k_r \rho_r$ are never any larger than about 2×10^{-5} for altitudes above 20 kilometers, they can be neglected and

$$\Delta h_g \approx \Delta h_a - r_e (k_b \rho_b - k_r \rho_r)$$

where

$$\Delta h_g = h_{g_b} - h_{g_r} \text{ and } \Delta h_a = h_{a_b} - h_{a_r}$$

Substituting for ρ_b from Equation 2-36

$$\Delta h_g \approx \Delta h_a - k_r \rho_r r_e (K e^{-b\Delta h_g} - 1) \qquad (2\text{-}39)$$

Since

$$e^{-b\Delta h_g} \approx 1 - b\Delta h_g \text{ for } b\Delta h_g \ll 1 \qquad (2\text{-}40)$$

Equation 2-39 may be expressed as

$$\Delta h_g \approx \frac{\Delta h_a - k_r \rho_r r_e^{(K-1)}}{1 - K b k_r \rho_r r_e} \qquad (2\text{-}41)$$

To determine the required constraint on the apparent height difference, use is first made of Equation 2-15 to obtain

$$\Delta h_a = h_{a_b} - h_{a_r} = r_s \left[\sin(Z_b) - \sin(Z_r)\right] \qquad (2\text{-}42)$$

where Z_b and Z_r are the zenith angles shown in Figure 2-7. Note in Figure 2-7 that Equation 2-42 may be expressed in terms of the angles E_b and E_r instead of the zenith angles as follows

$$\Delta h_a = r_s \cos(E_b) - \cos(E_r)$$

$$\Delta h_a = 2 r_s \sin \tfrac{1}{2}(E_b + E_r) \sin \tfrac{1}{2}(E_r - E_b)$$

Since $\delta = E_r - E_b$ and $E_r \approx E_b$

$$\Delta h_a \approx \delta r_s \sin(E_r) \qquad (2\text{-}43)$$

Note that Equation 2-43 could have been obtained by inspection of Figure 2-7 since Δh_a is the distance subtended by δ at a satellite-to-horizon distance of $r_s \sin(E_r)$. Substituting Equation 2-43 into Equation 2-41 yields the desired constraint on the grazing height difference

$$\Delta h_g = \frac{\delta\ r_s\ \sin(E_r) - k_r\ \rho_r\ r_e\ (K-1)}{1 - K\ b\ k_r\ \rho_r\ r_e} \qquad (2\text{-}44)$$

Using the approximation of Equation 2-40 in Equation 2-37, substituting the expression for Δh_g from Equation 2-44 into Equation 2-37, and substituting the equivalent expression for ρ_r in accordance with Equation 2-35, yields the following desired expression for the dispersion observed by a satellite:

$$\delta = \delta_\ell / C \qquad (2\text{-}45)$$

where δ_ℓ is given in Equation 2-38 and

$$C = 1 + K\ b\ R_r \left[r_s \sin(E_r) - \left(r_e / 2\pi b \right)^{\frac{1}{2}} \right] \qquad (2\text{-}46)$$

An indication of how well Equation 2-45 indicates the dispersion for a realistic atmosphere, such as the 1976 U.S. Standard Atmosphere, is shown in Table 2-5 where the results are shown along with those generated by

Table 2.5. Observed Dispersion Between 0.35 and 0.7 Microns for U.S. Standard Atmosphere and Two Satellite Altitudes

Grazing Height* (km)	Refraction* (arcsec)	Local Dispersion (arcsec)	Satellite Alt. = 1000 km			Satellite Alt. = 20,000 km		
			C	Dispersion (arcsec)		C	Dispersion (arcsec)	
				Eq. 2-45	Ray Trace		Eq. 2-45	Ray Trace
20	333.76	12.494	1.97	6.345	6.437	7.88	1.586	1.602
25	148.13	5.545	1.42	3.906	3.879	3.99	1.391	1.382
30	67.27	2.518	1.19	2.124	2.115	2.32	1.084	1.076
35	30.69	1.149	1.08	1.059	1.050	1.60	0.716	0.702
40	14.07	0.527	1.04	0.508	0.501	1.26	0.417	0.409
45	6.70	0.251	1.02	0.247	0.245	1.12	0.224	0.221
50	3.34	0.125	1.01	0.124	0.123	1.05	0.119	0.117

* For λ = 0.7 microns

accurate ray tracing[11]. The values of b and R_r used to generate the results with Equation 2-45 are those given for the 1976 U.S. Standard Atmosphere.

Note that, for a given grazing height, the magnitude of the factor C increases with satellite altitude, thereby reducing the magnitude of the observed dispersion. However, as previously noted, the dispersion can be measured very accurately with a two-color refractometer. The potential accuracy of this device is a function of various parameters such as telescope aperture size, star brightness, and optical transmission characteristics. Tests conducted by the University of Maryland have indicated an accuracy better than 0.001 arc second.

As previously indicated in Section 2.2, the dispersion measurement can be converted to an equivalent refraction measurement. Equation 2-45 provides a fairly good indication of what the relationship would be between the dispersion for two wavelengths (red and blue) and the refraction R_r for the red wavelength. It will be recalled that the locus of constant refraction may be visualized as an earth-based cone extending out into space, thereby permitting a relatively simple relationship between refraction and satellite position. Such is not the case for dispersion since the locus of constant dispersion is a more complicated surface in space. However, by converting the dispersion measurement to an equivalent refraction measurement, one can make use of the latter's relatively simple cone geometry to relate the dispersion measurement to satellite position.

A fairly good indication of the equivalent refraction is obtained by inverting Equation 2-45:

$$R_r = \frac{\delta}{K-1 - Kb\delta \left[r_s \sin(E_r) - (r_e/2\pi b) \frac{1}{2} \right]} \frac{1}{2} \qquad (2\text{-}47)$$

The error relationship between dispersion and its equivalent refraction is obtained by differentiating either Equation 2-47 or 2-45:

$$dR_r = \frac{K-1}{G^2} d\delta = \frac{C^2}{K-1} d\delta \qquad (2\text{-}48)$$

where G is the denominator of Equation 2-47 and C is the denominator of Equation 2-45.

Substituting the last expression in Equation 2-48 for dR in Equation 2-33 yields the following relationship between the errors in dispersion, atmospheric density modelling and vacuum tangent height:

$$dh_v = H \frac{d\rho_o}{\rho_o} + \left[(H\, r_e/2\pi) \frac{1}{2} - H/R_r - \left| \underline{r} \cdot \underline{u}_s \right| \right] \frac{C^2}{K-1} d\delta \qquad (2\text{-}49)$$

Substituting b = 1/H and assuming $r_s \sin(E_r) \approx \left| \underline{r} \cdot \underline{u}_s \right|$, one can use the relationship of Equation 2-46 to re-express the bracketed expression of Equation 2-49 so that

$$dh_v = \frac{1}{b} \left[\frac{1}{\rho_o} d\rho_o - \frac{C^2 (C + K - 1)}{K R_r (K - 1)} d\delta \right] \qquad (2\text{-}50)$$

The sensitivity of dispersion measurement to satellite position (e.g., h_v) is:

$$\frac{\partial \delta}{\partial h_v} = - \frac{K\ b\ R_r\ (K - 1)}{C^2\ (C + K - 1)} \qquad (2\text{-}51)$$

Figure 2-8 shows how well the sensitivity values generated by Equation 2-51 compare with those obtained by differentiating the ray trace data with a "5-point derivative" formula for a satellite at two different altitudes. Note that the ray trace curves in Figure 2-8 contain some high frequency oscillation due to differentiation of the discrete data associated with a multi-layered atmospheric model consisting of 72 levels between 14 km and 100 km altitude. Also note that the maximum sensitivity for the higher-altitude satellite occurs at a higher grazing height than that for the lower-altitude satellite. By differentiating Equation 2-51 it is found that the maximum sensitivity occurs when

$$C^2 + \left(2 - \frac{K}{2}\right) C + K - 1 = 0 \qquad (2\text{-}52)$$

For the wavelengths being considered in this report (λ = 0.35 and 0.7 microns), Equation 2-52 is satisfied when

$$C = -0.02485,\ 1.5061 \qquad (2\text{-}53)$$

where only the latter value is realizable. Substituting this value of C into Equation 2-46 yields the associated value of red-wavelength refraction in radians (denoted as R_r'):

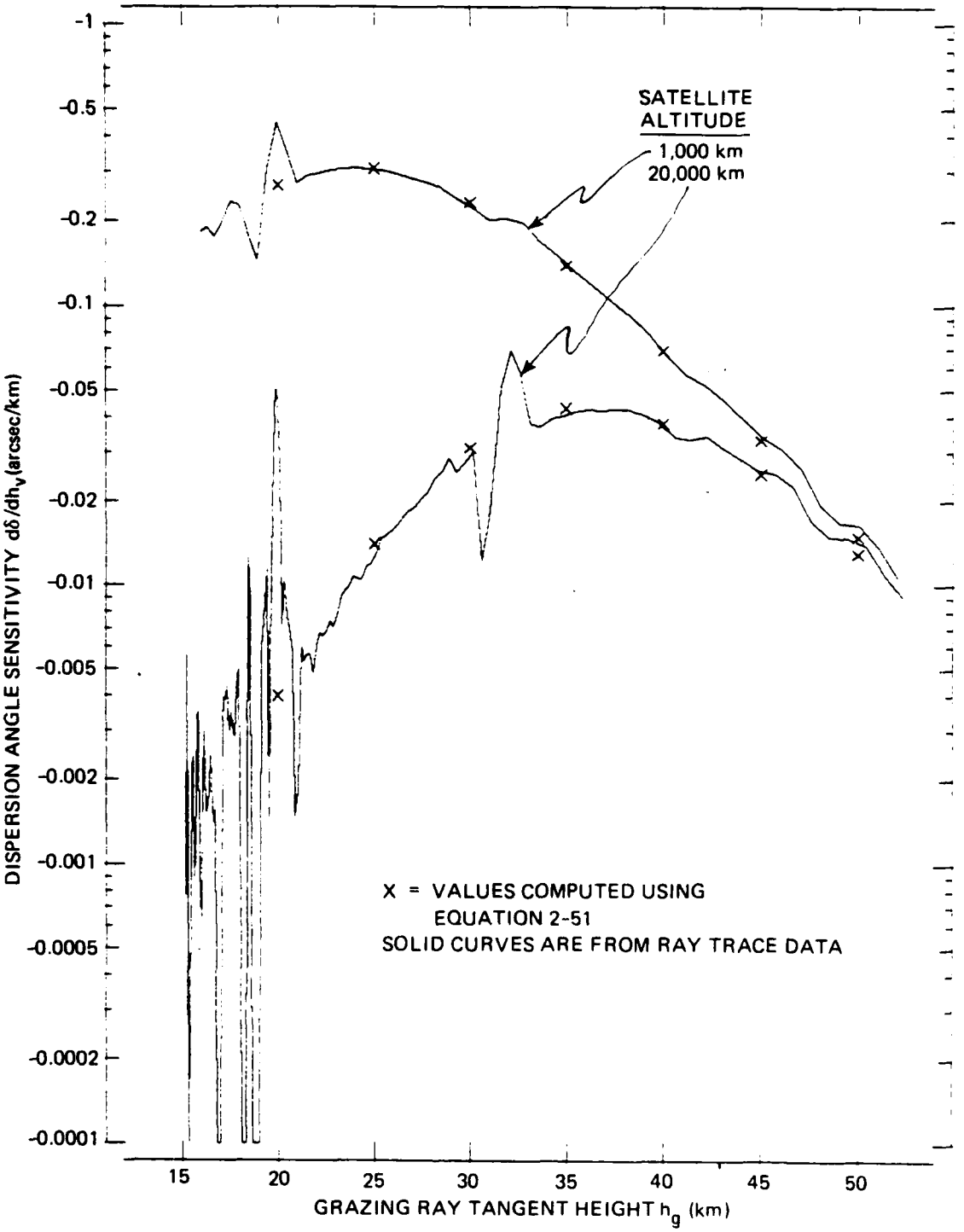

Figure 2-8. Dispersion angle sensitivity vs grazing ray tangent height

$$R_r' = 0.48787/b \left[r_s \sin(E_r) - \left(r_e/2\pi b \right)^{\frac{1}{2}} \right] \qquad (2\text{-}54)$$

If an exponential atmosphere is assumed, the grazing height (h_g'), where maximum dispersion sensitivity occurs, may be determined by substituting R_r' for R in Equation A-6:

$$h_g' = h_o - \frac{1}{b} \ln \left[\frac{0.48787}{b\, k_r\, \rho_o \left(2\pi b\, r_e \right)^{\frac{1}{2}} \left[r_s \sin(E_r) - \left[\frac{r_e}{2\pi b} \right]^{\frac{1}{2}} \right]} \right] \qquad (2\text{-}55)$$

where ρ_o is the density specified at some arbitrary height (h_o) in the exponential atmosphere. Using ρ_o = 40.084 g/m^3 at h_o = 25 km from the 1976 U.S. Standard Atmosphere, the values of h_g' computed for satellite altitudes of 1,000 and 20,000 km are 23.8 and 36.3 km, respectively.

SECTION 3

ERROR ANALYSIS

3.1 Introduction

3.1.1 Objectives

In choosing an error model, the following objectives were considered.

1) Determination of the navigator's steady state performance (position error standard deviations) assuming certain baseline parameters for its measurement capabilities.

2) Sensitivity analysis of the navigator to changes in the number and direction of star sightings and to changes in atmospheric modeling.

3) Estimation of the navigator's settling time (time for the position error standard deviations to approach their nominal steady state values).

Review of these goals led to the selection of a linearized Kalman filter. This filter is fundamentally the same algorithm as would be incorporated in the estimator of the actual navigation system.

3.1.2 Filter

The Kalman filter is a numerical algorithm which recursively estimates the current state of a system, $\underline{x}$, given external measurements, $\underline{z}$. The algorithm incorporates models of the system and measurement dynamics, and assumed statistics of system noises and measurement errors, to produce estimates which minimize the mean-squared errors (variances) of the state

variables. If the system is linear and its errors normally distributed, then the Kalman filter is truly the optimal estimator (see Gelb[14]).

The discrete linearized Kalman filter, the estimator chosen for this analysis, is shown in Table 3-1. The non-linear system of orbital motion is linearized about a reference trajectory which nominally describes the time history of the state variables; the state vector and covariance matrix are then propagated along this path; this filter provides a nearly optimal estimate of the non-linear system with considerably less computation than more accurate non-linear filters.

A fundamental component of the Kalman filter is the covariance matrix, P_i. The diagonal terms of P_i are the error variances of the state variables; off-diagonal terms are the covariances between pairs of state variables. The elements of the covariance matrix, especially the diagonal terms, provide a yardstick for determining how precisely the filter is estimating the state.

A very valuable property of the Kalman filter is that the error covariance matrix can be propagated and updated without estimating the state itself. This represents a significant saving in computer time compared to other techniques. Such covariance analyses have become widely accepted tools in analysing system performance.

3.2 System Description

3.2.1 States

The linearized state of the navigator may be described by seven elements: three components of position error, three components of velocity error and a scalar measurement bias error. These elements form the state vector

Table 3-1. Discrete Linear Kalman Filter.

System Model	$\underline{x}_k = \Phi_{k-1}\underline{x}_{k-1} + \underline{w}_{k-1}; \quad \underline{w}_k \sim N(0, Q_k)$
Measurement Model	$\underline{z}_k = \underline{h}_k(\underline{x}(t_k)) + \underline{v}_k; \quad \underline{v}_k \sim N(0, R_k)$
Initial Conditions	$E\,\underline{x}(0) = \underline{x}_0; \quad E\,\underline{x}(0)\underline{x}^T(0) = P_0$
Other Assumptions	$E\,\underline{w}_k\underline{v}_j^T = 0$ for all j,k Nominal trajectory $\bar{\underline{x}}(t)$ is available
State Estimate Extrapolation	$\underline{x}_k(-) = \Phi_{k-1}\underline{x}_{k-1}(+)$
Error Covariance Extrapolation	$P_k(-) = \Phi_{k-1}P_{k-1}\Phi_{k-1}^T + Q_{k-1}$
State Estimate Update	$\hat{\underline{x}}_k(+) = \hat{\underline{x}}_k(-) + K_k\,\underline{z}_k - \underline{h}_k(\bar{\underline{x}}(t_k)) - H_k(\underline{x}(\bar{t}_k))\,\underline{x}_k(-) - \underline{x}(\bar{t}_k)$
Error Covariance Update	$P_k(+) = I - K_k H_k(\underline{x}_k(t_k))\,P_k(-)$
Kalman Gain Matrix	$K_k = P_k(-)H_k^T(x(t_k))$ $H_k(\bar{\underline{x}}_k(t_k))P_k(-)H_k^T(\bar{\underline{x}}_k(t_k)) + R_k^{-1}$
Definition	$H_k(x(t_k)) = \left.\frac{\partial \underline{h}_k(\underline{x}(t_k))}{\partial \underline{x}(t_k)}\right\|_{\underline{x}(t_k)=\bar{\underline{x}}(t_k)}$

$$\underline{x} = \begin{bmatrix} \delta\underline{r} \\ \delta\underline{v} \\ \delta b \end{bmatrix} \qquad (3\text{-}1)$$

with the error covariance matrix

$$P = E\{\underline{x}\ \underline{x}^T\} \qquad (3\text{-}2)$$

where $\delta\underline{r}$ and $\delta\underline{v}$ define the errors in the trajectory estimated by the navigator. Their units are kilometers and kilometers/second, respectively.

The scalar measurement bias error was introduced as an additional variable in the above state to account to some extent for bias-type errors in atmospheric modeling and refraction or dispersion measurements. The addition of this variable to the estimated state permits the navigator to remove its effect from the estimated position and velocity. It should be noted, however, that the addition of this state variable (and its associated variance) adds complexity and randomness to the system and so increases the size of the position and velocity error variances compared to the case where no bias error is present. In the present study this bias error is treated as the overall bias error in the measurement of vacuum tangent height resulting from systematic errors in atmospheric modeling and refraction or dispersion measurements. In Section 2.4.5 the relationship between errors in vacuum tangent height, atmospheric modeling and refraction measurement are given for an exponential atmosphere. This relationship indicates that a more elaborate representation of systematic error could have been included in the present analysis (i.e. separate systematic errors for density, refraction and density scale height). However, for the purposes of this preliminary investigation, it was felt that the use of a bias error in vacuum tangent height was sufficient.

3.2.2 Coordinate Systems

The satellite's position and velocity may be described in earth-centered inertial (ECI) coordinates. The z axis points north along the Earth's polar axis, the x axis points in the direction of the vernal equinox and the y axis completes a right-handed coordinate system. This system is the one ultimatly used to propagate and update the covariance matrix.

While the ECI coordinate system is convenient for computation, the position uncertainties and update directions are more readily visualized in terms of the satellite-centered coordinate system TNR (Tangential, Normal, Radial) shown in Figure 3-1. In this system $\underline{u}_R$ points toward the earth along the local vertical, $\underline{u}_N$ is normal to the orbital plane and points in the opposite direction of the satellite's orbital angular momentum vector; $\underline{u}_T$ is orthogonal to $\underline{u}_R$ and $\underline{u}_N$ and is directed in the same sense as the satellite's velocity vector. In Figure 3-1 the direction of a star ($\underline{u}_S$) undergoing refraction can be specified in TNR coordinates by an azimuth angle (ϕ) and elevation angle (θ) where the latter is also shown in Figure 3-2.

The direction of satellite position update for the star in Figures 3-1 and 3-2 is given by the unit vector $\underline{u}_{up}$ where

$$\underline{u}_{up} = \cos\theta \left(\cos\phi\ \underline{u}_T + \sin\phi\ \underline{u}_N\right) - \sin\theta\ \underline{u}_r \qquad (3\text{-}3)$$

The relationship between the ECI and TNR coordinate systems is given by

$$\underline{r}^{TNR} = C_{ECI}^{TNR}\ \underline{r}^{ECI} \qquad (3\text{-}4)$$

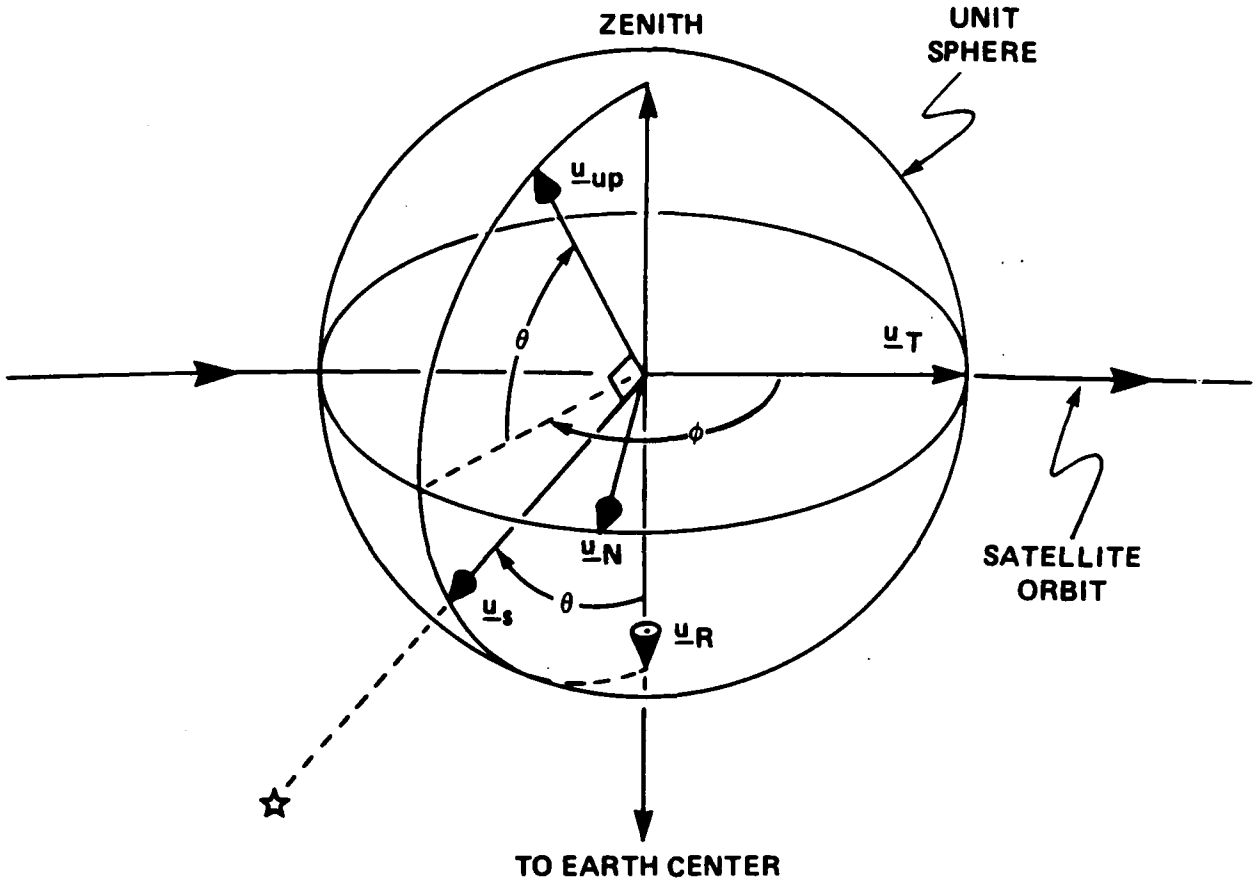

Figure 3-1. Satellite-Centered Coordinate System

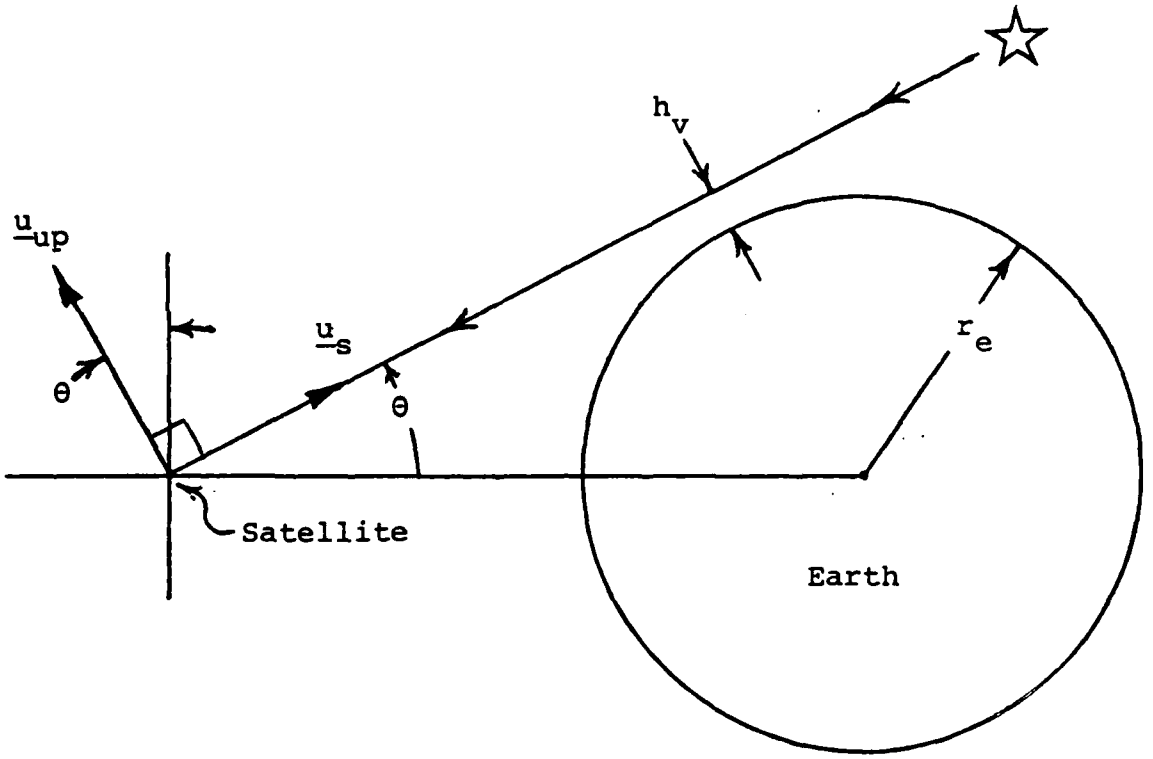

Figure 3-2. Definition of Elevation Angle (θ)

where

$$C_{ECI}^{TNR} \equiv \begin{bmatrix} \text{unit } (\underline{r} \times (\underline{v} \times \underline{r}))^T \\ \text{unit } (\underline{v} \times \underline{r})^T \\ \text{unit } (-\underline{r})^T \end{bmatrix} \qquad (3\text{-}5)$$

The transformation for the full state vector is given by

$$\underline{x}^{TNR} = C^* \underline{x}^{ECI} \qquad (3\text{-}6)$$

where

$$C^* \equiv \left[\begin{array}{c|c|c} C_{TNR}^{ECI} & 0 & \\ \hline 0 & C_{TNR}^{ECI} & 0 \\ \hline & 0 & 1 \end{array}\right]_{7\times 7} \qquad (3\text{-}7)$$

Note that the measurement bias, a scalar, is not affected by the transformation of coordinates.

3.3 Propagation

3.3.1 State Transition Matrix

The state transition matrix $\Phi(t,t_0)$ permits the direct and simple linear calculation of the state vector at time t given the state at time t_0, provided that the system is unforced during that time interval.

Thus,

$$\underline{x}(t) = \Phi(t,t_0)\underline{x}(t_0) \tag{3-8}$$

Similarly, the error covariance matrix P at time t_0 may be propagated to time t using

$$P(t) = \Phi(t,t_0)P(t_0)\Phi^T(t,t_0) \tag{3-9}$$

Let $\underline{x}$ be the navigator's reduced state vector (position and velocity) and $\Phi^*(t,t_0)$ be the corresponding transition matrix between time t and t_0. Let

$$G(t) = \left.\frac{\partial \underline{g}}{\partial \underline{r}}\right|_{\underline{r}=\underline{r}_{ref}} \tag{3-10}$$

where

$\underline{g}$ = local gravitational acceleration

$\underline{r}_{ref}$ = reference trajectory

and

$$F(t) = \left[\begin{array}{c|c} 0 & I \\ \hline G(t) & 0 \end{array}\right]_{6\times 6} \tag{3-11}$$

Then $\Phi^*(t,t_0)$ is the solution of the matrix differential equation

$$\frac{d}{dt}\Phi^*(t,\ t_0) = F(t)\Phi^*(t,\ t_0) \tag{3-12}$$

subject to the initial conditions

$$\Phi^*(t_0,\ t_0) = I_{6\times 6} \tag{3-13}$$

These equations may be solved in closed form, using methods described by Goodyear[15].

The transition matrix for the full state vector $\underline{x}$ is related to the reduced state transition matrix by

$$\Phi(t,t_0) = \left[\begin{array}{c|c} \Phi^*(t,t_0) & 0_{6\times 1} \\ \hline 0_{6\times 1} & 1 \end{array}\right] \qquad (3\text{-}14)$$

Note that the estimate of the measurement error bias remains constant during the transition.

3.3.2 Process Noise

Disturbing accelerations strongly affect the long term behavior of an orbit. Such disturbances[16] are introduced by the higher-order gravity field terms, atmospheric drag, solar pressure, etc. To correctly model these effects in the present study would be computationally expensive and somewhat unnecessary. Therefore, these disturbances were treated as process noise driving the unforced continuous system, i.e.

$$\dot{\underline{x}} = F\underline{x} + \underline{w} \qquad (3\text{-}15)$$

where

$\underline{x}$ = system state vector

$\underline{w}$ = unmodeled disturbance vector

and

$$w = \begin{bmatrix} 0_{3x1} \\ \underline{w}_{\underline{v}\ 3x1} \\ 0_{1x1} \end{bmatrix} \tag{3-16}$$

since the noises (disturbing accelerations) directly act on the velocities only. These noises are treated as white and unbiased, with the spectral density Q for the discrete case given as

$$Q = E\{\underline{w}\ \underline{w}^T\} \tag{3-17}$$

The propagation of the error covariance matrix is similarly disturbed by an additive term

$$P_{i+1} = \Phi(t_{i+1}, t_i) P_i \Phi^T(t_{i+1}, t_i) + Q_i \tag{3-18}$$

where Q_i is the covariance matrix of the process noise.

Formally, the transition from the noise spectral density matrix to the noise covariance matrix is given by

$$Q_i = \int_{t_i}^{t_{i+1}} \Phi(t_{i+1}, \tau) Q(\tau) \Phi^T(t_{i+1}, \tau) d\tau \tag{3-19}$$

However, for small time step Δt this equation can be approximated by

$$Q_i = Q\Delta t \tag{3-20}$$

(see Schweppe[17]).

3.4 Measurement Incorporation

The linear Kalman filter requires that the system measurements $\underline{z}$ be linear combinations of the current state $\underline{x}$ and a random measurement error, $\underline{e}$.

$$\underline{z}_i = H_i \underline{x}_i + \underline{e}_i \tag{3-21}$$

The error covariance matrix P_i is updated using only the measurement matrix H_i.

$$P_i(+) = \left(I - K_i H_i\right) P_i(-) \left(I - K_i H_i\right)^T + K_i R_i K_i^T \tag{3-22}$$

where

$$K_i = P_i(-) H_i \left(H_i P_i(-) H_i^T + R_i\right) \tag{3-23}$$

and

$$R_i = E\left(\underline{e}_i \underline{e}_i^T\right) \tag{3-24}$$

What follows are derivations of the matrices required for the covariance update.

3.4.1 Measurement Matrix

By observing starlight refraction through the atmosphere, the navigator effectively measures the vacuum tangent height with an unknown measurement bias b. Thus

$$z = h_v + b \tag{3-25}$$

The bias and its variance may not be the same everywhere and some consideration is given to its treatment in Section 4.3.1.3.

According to Equation 2-21

$$h_v = \underline{r} \cdot \underline{u}_p - r_e \tag{3-26}$$

where

$\underline{r}$ = satellite position

r_e = earth radius

and $\underline{u}_{up}$ is the update direction (Equation 2-20) given by

$$\underline{u}_{up} = \text{Unit}\left[(\underline{u}_s \times (\underline{r} \times \underline{u}_s\right] \tag{3-27}$$

By definition

$$H = \frac{\partial z}{\partial \underline{x}} \tag{3-28}$$

where $\underline{x}$ is the non-linearized state vector

$$\underline{x} = \begin{bmatrix} \underline{r} \\ \underline{v} \\ b \end{bmatrix} \tag{3-29}$$

Since z is not a function of velocity

$$H = \left[\frac{\partial h_v}{\partial \underline{r}} \;\vdots\; 0_{1\times 3} \;\vdots\; 1\right]_{1\times 7} \tag{3-30}$$

Solving for the measurement gradient with respect to position:

$$\frac{\partial h_v}{\partial \underline{r}} = \underline{r}^T \left(\frac{\partial \underline{u}_{up}}{\partial \underline{r}} \right) + \underline{u}_{up}^T \qquad (3\text{-}31)$$

It can be shown, however, that the gradient vector $\left(\frac{\partial \underline{u}_{up}}{\partial \underline{r}} \right)$ is normal to $\underline{r}$, i.e.

$$\underline{r}^T \left(\frac{\partial \underline{u}_{up}}{\partial \underline{r}} \right) = 0 \qquad (3\text{-}32)$$

Therefore,

$$H = \left[\underline{u}_{up}^T \;\vdots\; 0_{1\times 3} \;\vdots\; 1 \right]_{1\times 7} \qquad (3\text{-}33)$$

3.4.2 Measurement Error Matrix

Since the navigator's measurement is a scalar, the measurement error matrix R_i (see Equation 3-24) contains only the single variance associated with the error in estimating the vacuum tangent height h_v, i.e.

$$R_i = \sigma_{h_v}^2 \qquad (3\text{-}34)$$

SECTION 4

IMPLEMENTATION

4.1 Programs

Two different computer programs, arbitrarily designated as SHAD1 and SHAD2, were developed to implement the Kalman filter described in Section 3; each used a different means to simulate star sightings and orbital trajectories. By comparing the results of SHAD1 with those of SHAD2, one can judge the validity of the assumptions made in each.

4.1.1 SHAD1

SHAD1 used the the following approximations in its implementation of the navigation filter.

1) The satellite's orbit is Keplerian.

2) Times and directions (in satellite-centered coordinates) of measurement stars (those appearing close to the horizon) were randomly generated.

3) The covariance matrix was propagated and updated only at uniformly spaced time intervals.

SHAD1 did not utilize a catalog of star positions in terms of celestial coordinates. Rather, the program selected a number of random sighting times where the satellite would observe a grazing star. For each sighting

time, an independently generated random star direction was assigned which placed the star at a specified tangent height when viewed from the satellite. The sighting times and star directions were generated in a manner which is consistent with the probability distribution expected of measurements taken from a uniformly distributed star field.

4.1.2 SHAD2

SHAD2 used more realistic assumptions for the navigator than SHAD1.

1) Any trajectory can be used, provided the positions and velocities are given for the times of interest.

2) Star directions for measurements were obtained from the Yale University Catalog of Bright Stars.

3) The covariance matrix was propagated between irregularly spaced time intervals corresponding to the times between actual measurements.

4.2 Progagation

4.2.1 Trajectories

Both SHAD1 and SHAD2 required a nominal trajectory (time, position, and velocity of the satellite at frequent intervals) about which to propagate the error covariance matrix. Auxiliary programs were used to generate the trajectory files for the two filter programs. For SHAD2, use was made of the Goddard Trajectory Determination System (GTDS)[18] to generate satellite trajectories perturbed by the dominant higher-order gravitational term J_2.

4.2.2 State Transition Matrices

Propagation of the covariance matrix between updates was accomplished with state transition matrices computed for the time steps required. A technique developed by Goodyear[15] was used to calculate the state transition matrices for the Keplerian orbits of SHAD1.

Since the direct calculation of state transition matrices for the perturbed orbits of SHAD2 was considered to be very costly, a method of patched conics was utilized to obtain an approximate solution. Insofar as propagation of the covariance matrix is relatively insensitive to small changes in the state transition matrix, this approximation was considered to be satisfactory. Given a description of a perturbed orbit with closely spaced time steps, the method of patched conics was used as follows. The instantaneous position and velocity of a satellite describes a Keplerian orbit which is tangent to the satellite's actual path at that point. Over a short time interval this instantaneous conical path, or osculating orbit, remains very close to the perturbed trajectory. By calculating the osculating orbits for all known points in the perturbed orbit, one can approximate the true trajectory with one consisting of a series of conical orbits patched together[19]. The state transition matrices along these osculating orbits are readily calculated with the technique employed in SHAD1.

4.2.3 Estimation of Process Noise

As previously indicated in Section 3.3.2, a process noise was included in the linearized filter to statistically account for the un-modeled disturbing accelerations due to air drag, solar pressure and the higher order gravitational terms. This noise was estimated by first sampling the

disturbing accelerations indicated by the GTDS program at discrete times throughout the satellite orbit and estimating the variances of the samples in TNR coordinates. A spectral density matrix Q was then formed, with all of its non-zero diagonal elements being assigned the value of the largest variance component. This assured that the probability distribution of the process noise would be spherical and large enough to conservatively model the system. From the spectral density matrix, the process noise covariance matrix Q_i was calculated as shown in Equation 3-20.

It should be noted that the process noise used in this study included the effects of all higher order gravitational terms of the Goddard Earth Model Number 9 (GEM9) except for the dominant oblateness term J_2 whose effect was already included in the generation of satellite trajectories for SHAD2. This process noise was used in the generation of performance results for both SHAD1 and SHAD2. Consequently, the performance results of SHAD1 are those for the case where the precession effect of J_2 is assumed to be non-existent, while those of SHAD2 do include its effect. An actual navigator would probably incorporate the dynamics of J_2, and possibly some additional terms, in the state transition matrix and treat all other disturbances as process noise. However, for the purposes of the present covariance analysis, it was felt that the performance results would be fairly indicative of what one can expect.

4.3 Measurements

4.3.1 Measurement Parameters

4.3.1.1 Number of Stars

The number of star sightings, and hence the number of covariance updates, performed during an orbital revolution is primarily dependent on the brightness limits of the navigator's star sensor. As the navigator's sensitivity is improved, more stars can be acquired for navigation. This can be simulated in the program by varying the number of star positions made available for covariance updates.

SHAD1 requires the user to enter the number of stars in the sky which are detectable (i.e. of sufficient brightness) to the navigator. SHAD1 then estimates the average number of stars that the navigator can expect to view during a single orbital rotation and generates the appropriate number of star sighting directions.

SHAD2 employs the Yale University Catalog of Bright Stars to describe its star field and uses brightness limits to decide whether or not an individual grazing star will be sighted. If not, the program will continue covariance propagation through the time that a star sighting might have been made.

4.3.1.2 Azimuth Span

The azimuth span specifies how much and what part of the horizon will be scanned for grazing stars (see Figure 4-1). Increasing the width of this span places more stars within the navigator's field of view. For applications requiring extreme accuracy this span should encompass 360 degrees. In most cases the azimuth span may exclude the forward section of the horizon since rising stars are more difficult to locate before they leave the atmosphere. Stars near ±90 degrees azimuth will take much longer

to go into refraction than those close to the orbital plane. In the time taken to observe one star near ±90 degress it might be possible to observe two or more stars closer to the orbital plane. For this reason, most simulations use an azimuth span between 135 and 225 degrees.

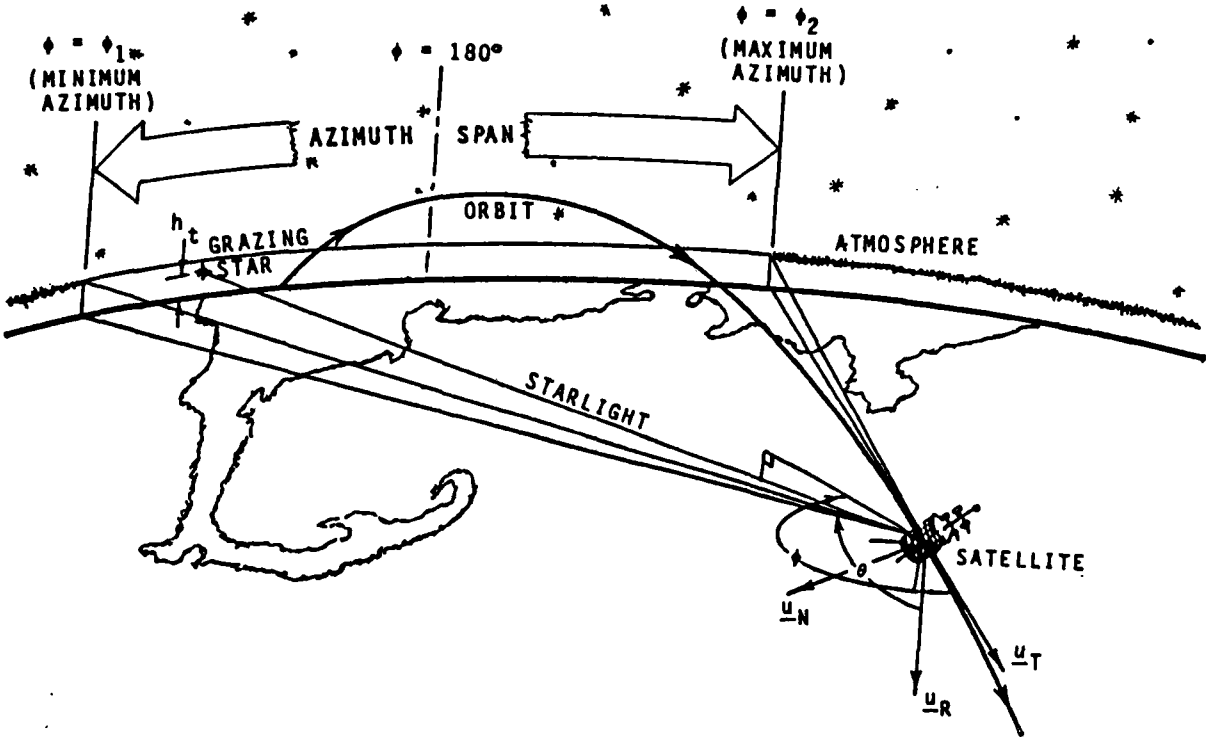

Figure 4-1. Description of azimuth span

4.3.1.3 Measurement Bias

The grazing latitude, ψ, is the earth latitude over which a particular ray of grazing starlight makes its closest approach to the surface. It is given by

$$\sin \psi = \underline{u}_{up} \cdot \underline{i}_z \qquad (4\text{-}1)$$

where $\underline{i}_z$ = earth's polar axis

and

$$\underline{u}_{up} = \text{Unit}\left[\underline{u}_s \times (\underline{r}_s \times \underline{u}_s)\right] \qquad (4\text{-}2)$$

Both SHAD1 and SHAD2 use the grazing latitude to model the measurements of atmospheric refraction in one of three different ways:

1) Bias Everywhere

The program treats every measurement as if it contained a bias which can be estimated. Measurements may be taken over any part of the earth. The measurement matrix H is always given by

$$H = \left[\underline{u}_{up}^T \;\vdots\; 0_{1x3} \;\vdots\; 1\right]_{1x7} \qquad (4\text{-}3)$$

2) No Bias, Measurements Limited

Refraction measurements are limited to those for which the grazing latitude falls within a band about the equator given by $\pm\psi_{max}$ (see Figure 4-2). Within this band atmospheric behavior is understood well enough to model measurements without a bias. Any star found to graze outside of this band will be ignored for measurements. Since a measurement bias is not observed during a measurement, the measurement matrix becomes

$$H = \left[\underline{u}_{up}^T \;\vdots\; 0_{1x3} \;\vdots\; 0\right]_{1x7} \qquad (4\text{-}4)$$

Without the observation of a bias, no cross correlation can be built up in the covariance matrix between the measurement bias variance and other state variances. The value chosen for the initial measurement bias variance can be arbitrary since it will not be changed by a measurement nor will it affect the other state variances. Effectively, the state of the system is reduced by one state variable.

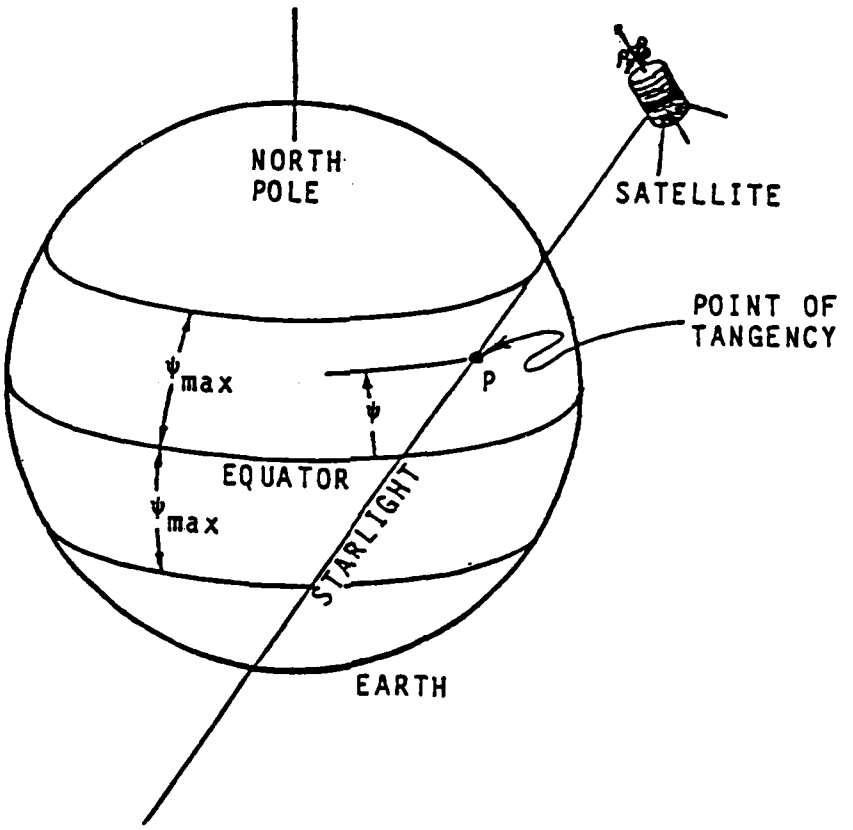

Figure 4-2. Measurement restrictions due to grazing latitude

In the cases tested, the maximum grazing latitude was set at 30 degrees for this option.

3) Latitude-Dependent Bias

Refraction measurements are made everywhere but measurements made outside of a specified equatorial band Ψ_{max} are treated as containing a bias while those inside are not. For an individual star sighting, if its grazing latitude is within the equatorial band then

$$H = [\underline{u}_{up}^T \mid 0_{1x3} \mid 0]_{1x7} \tag{4-5}$$

otherwise

$$H = [\underline{u}_{up}^T \mid 0_{1x3} \mid 1]_{1x7} \tag{4-6}$$

4.3.2 Simulated Star Field (SHAD1)

4.3.2.1 Description

The brighter stars visible from the Earth are distributed almost uniformly throughout the sky. This makes it possible to greatly simplify the simulation by updating the filter with artificially generated star sightings. The artificial star field should yield approximately the same navigator performance as an actual star field.

These random, artificially generated star positions need not be specified in inertial space. Suppose we have arbitrarily assigned a star. This star must be placed in the sky so that its light will graze at the desired tangent altitude. For convenience, let the star direction $\underline{u}_s$ be given in TNR coordinates. If we assume a spherical earth, the horizon elevation angle θ is specified by the satellite and vacuum tangent altitude (see Figure 3-2): a star's position can thus be defined given a sighting azimuth ϕ.

An artificial star field can be created by randomly assigning azimuths and a schedule of sighting times (tantamount to specifying positions in the known reference orbit). If desired, this data can be converted to represent star positions in ECI coordinates.

4.3.2.2 Probability Distribution

To simulate a realistic star field, the schedule of star sightings (sighting times and azimuths) must be consistent with the presumption that bright stars are uniformly distributed over the sky. Therefore, the probability distributions used to randomly generate sighting times and azimuths must be such that they conform to a uniform star field when converted to ECI coordinates.

Circling about the earth, the navigator observes stars near the horizon moving into and out of refraction. If its orbit is circular the navigator has a constant expectation of viewing a grazing star anywhere in the orbit. In this case, the orbital angular positions of the satellite when star sightings occur will be uniformly distributed between 0 and 360 degrees. These angular positions can be readily converted into times when the navigator observes a star.

As the navigator scans the horizon within its azimuth span, it will, in the course of one orbital period, survey a sector of the celestial sphere (see Figure 4-3). It can be readily shown that the fraction of the celestial sphere scanned is given by

$$Fr = \frac{\sin \theta}{2} \left| \sin \phi_2 - \sin \phi_1 \right| \qquad (4\text{-}7)$$

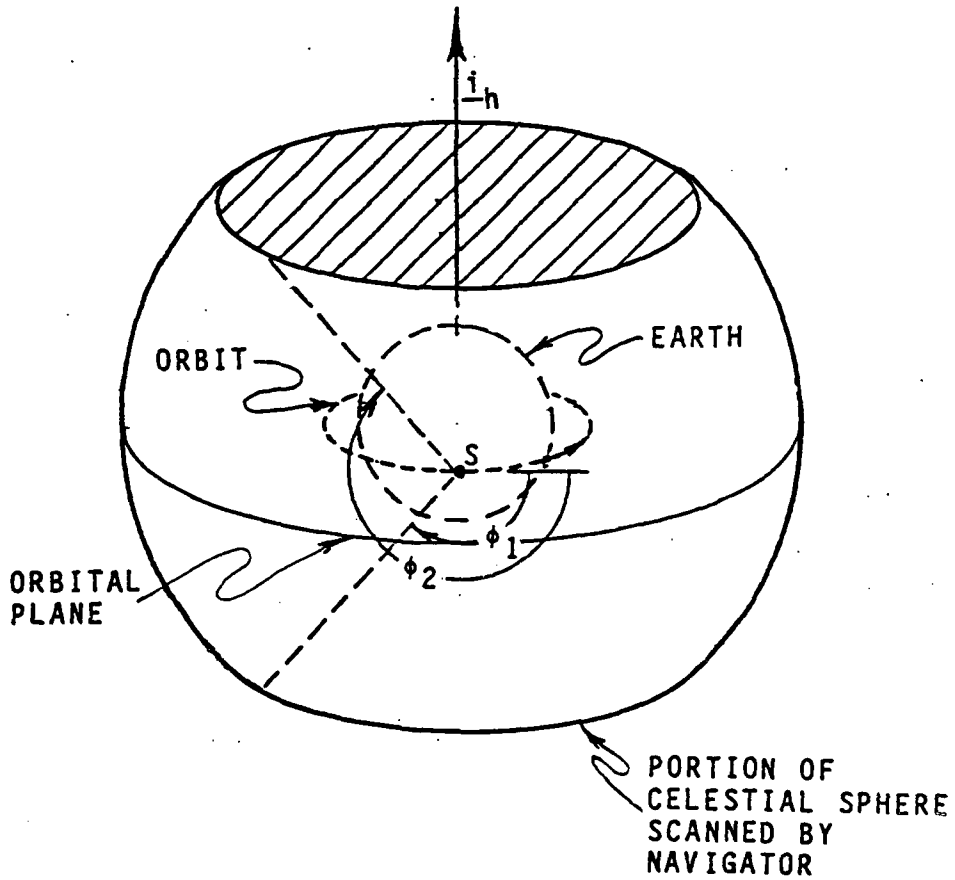

Figure 4-3. Sector of the celestial sphere scanned by navigator.

where ϕ_1 and ϕ_2 are the lower and upper limits of the azimuth span. Clearly, if we specify that there shall be N stars on the celestial sphere of sufficient brightness to be used by the navigator, then, on the average, only N^* of these will actually be usable during one orbital period where

$$N^* = Fr\ N \tag{4-8}$$

The distribution of star sightings as a function of azimuth may be derived by observing that the probability of observing a star within a narrow annular segment of width $d\phi$ is proportional to the area of that segment; the differential area depends upon its azimuth. It can be shown that the probability density of star sightings as a function of azimuth is

$$P(\phi) = \frac{\cos \phi}{\sin \phi_2 - \sin \phi_1} \qquad (4\text{-}9)$$

The user specifies the number of stars, N, which he wishes to place in the artificial sky and the azimuth span, ϕ_1 and ϕ_2, of the sensor. For a given orbit, SHAD1 estimates the number of stars that the sensor can expect to find within its azimuth span and generates that number of star sightings and directions for each orbit.

4.3.2.3 Sighting Times

Sighting times were created by generating random numbers uniformly distributed between 0 and 1. The random numbers are used to specify the fraction of the orbit traveled from the satellite's initial position. For a circular orbit, this fraction readily gives the time of flight since the satellite last passed its initial position. Sighting times for additional revolutions were obtained by adding the appropriate number of orbital periods.

4.3.2.4 Azimuth Angles

To generate random azimuth angles such that they have the probability distribution given in Equation (4-9), use was made of the probability function Pr ($\phi \leq \tilde{\phi}$). Let us consider the random variable

$$s = \Pr\left\{\phi \leq \tilde{\phi}\right\} \tag{4-10}$$

where $\tilde{\phi}$ is one of a random ensemble of azimuths having the desired distribution. By definition, s is uniformly distributed between 0 and 1. Furthermore, every value of s uniquely specifies a value for ϕ by

$$\phi = \sin^{-1}\left[s(\phi)\ (\sin\phi_2 - \sin\phi_1) + \sin\phi_1\right] + \begin{cases} 0 & |\phi| < \frac{\pi}{2} \\ \pi & \frac{\pi}{2} < \phi < \frac{3\pi}{2} \end{cases} \tag{4-11}$$

If we choose random numbers between 0 and 1 and assign them to s, the corresponding values of ϕ will have the proper distribution. For SHAD1, N random angles would be generated in this manner and paired with the randomly generated sighting times for each orbital revolution.

4.3.3 Real Star Field (SHAD2)

4.3.3.1 Star Catalog

The Yale University Catalog of Bright Stars lists 9091 stars according to position, type, and visual magnitude. From this catalog, a new catalog of 362 stars was created which contained those stars having a brightness of at least fourth magnitude as seen by an S-20 star sensor.

4.3.3.2 Estimation of Sighting Times

To estimate the time when a satellite can expect to see a star rise or set, the star's position was first converted to the orbital coordinate

system ($\underline{i}_p$, $\underline{i}_e$, $\underline{i}_h$) shown in Figure 4-4. The catalogued star's position as a unit vector $\underline{u}_s$ in ECI coordinates can be converted to orbital coordinates by the transformation

$$\underline{u}_s^* = \begin{bmatrix} \underline{i}_p^T \\ \underline{i}_e^T \\ \underline{i}_h^T \end{bmatrix} \underline{u}_s \qquad (4\text{-}12)$$

where $\underline{i}_p$, $\underline{i}_e$ and $\underline{i}_h$ are unit vectors defining the directions of the orbital coordinate axes in ECI coordinates. From this one can define the star's direction in terms of an orbital right ascension α (measured from the perigee direction, $\underline{i}_p$) and orbital declination δ (measured from the orbital plane) as follows:

$$\alpha = \tan^{-1}\left[u_{s_p}^* \Big/ u_{s_e}^* \right] \qquad (4\text{-}13)$$

$$\delta = \tan^{-1}\left[u_{s_h}^* \Big/ \left[u_{s_e}^{*2} + u_{s_p}^{*2} \right]^{\frac{1}{2}} \right] \qquad (4\text{-}14)$$

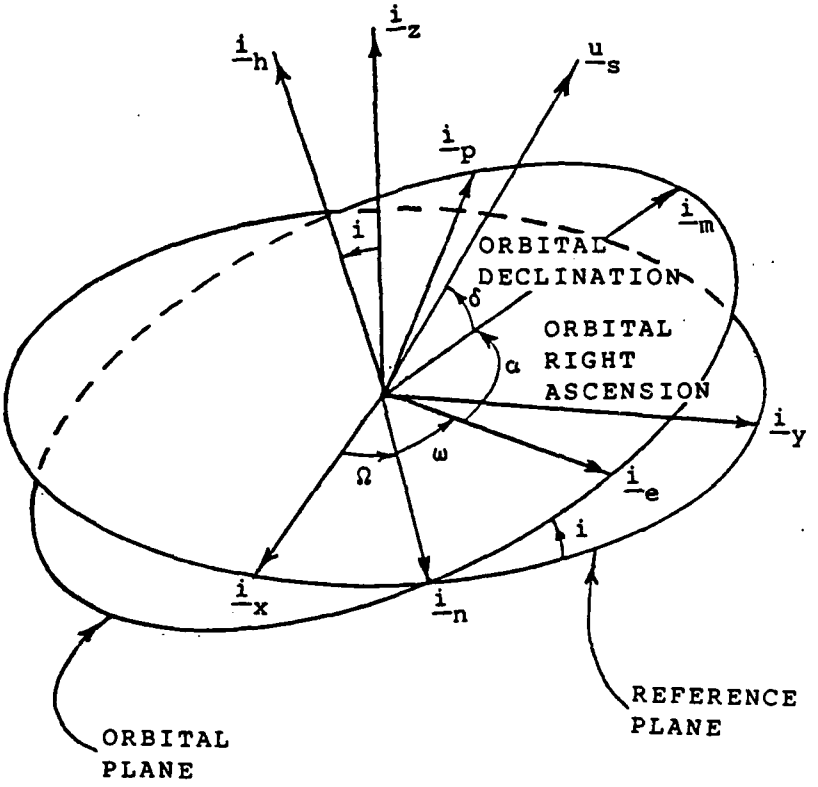

Figure 4-4. Orbital coordinates for star direction

For a particular orbit, the horizon elevation angle θ is given by

$$\sin \theta = \frac{(r_e + h_v)(1 + e \cos f)}{p} \qquad (4\text{-}15)$$

where

r_e = mean Earth radius

h_v = vacuum altitude of starlight

p = semi-latus rectum of orbit

e = orbital eccentricity

f = true anomaly (satellite angular position with respect to perigee)

To place the Earth directly between the satellite and the star, the satellite should be 180 degree from the projection of the star direction onto the orbital plane, i.e.

$$f = \alpha + \pi \qquad (4\text{-}16)$$

Substitution of this value of f into Equation 4-15 yields a value for θ which if greater than the star's orbital declination δ implies that the star will rise and set at the vacuum altitude h_v (see Figure 4-5). The angle δ shown in Figure 4-5 describes the angular half-width of the chord formed by the passage of a star behind the Earth. By spherical trigonometry

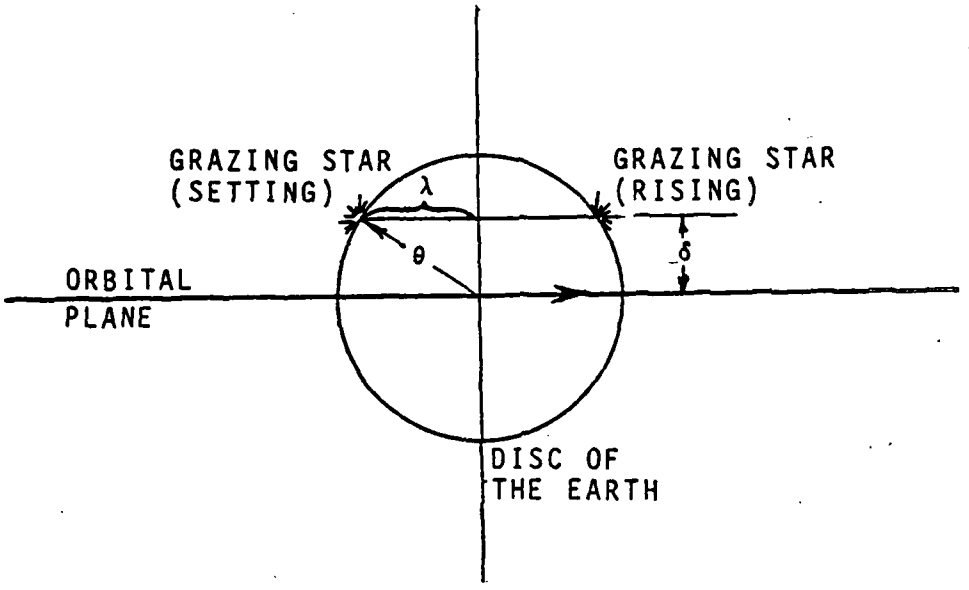

Figure 4-5. Selection of grazing stars

$$\cos \lambda = \cos \theta / \cos \delta \tag{4-17}$$

or, using the results of Equation 4-15,

$$\cos \lambda = \frac{1}{\cos \delta} \left[1 - \left[\frac{(r_e + h_v)(1 + e \cos f)}{p} \right]^2 \right]^{\frac{1}{2}} \tag{4-18}$$

In terms of the satellite's orbit (see Figure 4-6), f_S and f_R determine where the satellite should be in order to observe a particular star either rise or set at the tangent altitude h_v. For a rising star

$$f_R = \alpha + \pi + \lambda \tag{4-19}$$

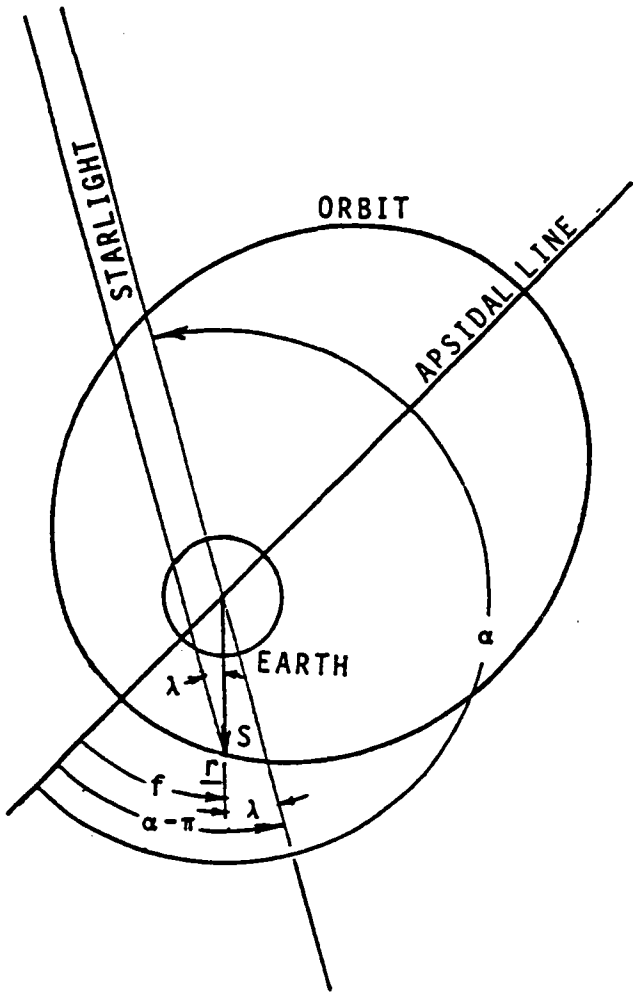

Figure 4-6. Orbital positions for observing a grazing star

and for a setting star

$$f_S = \alpha + \pi - \lambda \qquad (4\text{-}20)$$

The satellite angular position where the grazing star is observed may be solved recursively using Equations 4-18 and 4-19 or 4-20. From this the time for observing the star is calculated.

4.3.3.3 Effects of Orbital Precession

The estimate of satellite sighting times developed above presumes a stationary Keplerian orbit for at least one revolution. One can approximate the precise sighting times for a perturbed trajectory by considering only the effects of the zonal harmonic term J_2. Since J_2 dominates all other effects for low earth orbits, this corrected sighting time should assure that when the indicated star is sighted from a perturbed trajectory the vacuum altitude obtained should be very close to the one desired.

The presence of J_2 causes the orbit to precess about the Earth's polar axis. The amount of this precession during a single orbit is given by

$$\Delta\Omega = -3\pi\ J_2\ (r_{eq}/p)\ \cos i \qquad (4\text{-}21)$$

where

J_2 = gravitational potential term

r_{eq} = equatorial radius of the Earth

p = semi-latus rectum of the orbit

i = orbital inclination

To correct for orbital precession after each orbit, the orbital coordinate unit vectors ($\underline{i}_p$, $\underline{i}_e$, $\underline{i}_h$) used in Equation 4-12 were rotated about the Earth's polar axis by the amount given in Equation 4-21.

SECTION 5

NAVIGATION PERFORMANCE RESULTS

5.1 Introduction

Performance results were generated for three different satellite orbits which are considered to be fairly representative of those used today. All of the orbits were circular and had the following distinguishing characteristics:

Type Orbit	Altitude(km)	Inclination(deg)
Low Orbit	915	65
GPS	20,242	63
Geosynchronous	35,866	0

The sensitivity of performance to variation in measurement error and number of star sightings is presented for all of the above orbits. However, the effect of variation in other parameters is shown only for the low orbit and can be considered to be somewhat similar for the other orbits.

In most cases, only "setting" stars were used for navigation (i.e. stars in the aft direction of satellite motion). Such stars can be acquired before they undergo refraction which is much easier than acquiring stars coming out of refraction. However, since there are some performance benefits in using both setting and rising stars, data was also generated for this situation so that one can weigh those benefits against the additional difficulty in system design.

All star sightings for position update occurred when the ray grazing height was 25 kilometers. As previously indicated in Section 2.4.5, each star/horizon measurement was treated as an equivalent vacuum tangent height measurement so that the errors in atmospheric density modeling, and in dispersion or refraction measurement, could be expressed in common units of meters without being concerned with the relative contributions of each. Most of the performance results were generated with a baseline measurement error of 70 meters (one sigma) in vacuum tangent height, although some data was generated for other values.

The effect of a bias-type measurement error was also included in the study and was treated as an additional state parameter to be updated by the Kalman filter. Again, no strong distinction was made between the relative bias error contributions made by errors in atmospheric modeling and in dispersion or refraction measurement. However, most individuals feel that the major contributor will be atmospheric density modeling, and that systematic bias-like errors in atmospheric modeling will occur over temperate and polar regions. Most of the performance results are for the case where a bias error is present for all observations outside $\pm$ 30 degrees latitude. At the start of each navigation run, the uncertainty in the bias estimate was generally assumed to be 100 meters (one sigma). Preliminary studies indicated that larger initial bias uncertainties (up to 500 meters) had little effect on the final results.

It should be noted that the present treatment of a systematic atmospheric density error as only a bias type error is probably not the

best approach since one would expect systematic changes in the error as a function of season and geographical location. However, for the purposes of this study, it was felt that an equivalent bias in vacuum tangent height would be sufficient.

Three different measurement bias options were employed in the study and are as follows:

Option 1 - All measurements have no bias.

Option 2 - All measurements have the same bias which is to be estimated.

Option 3 - All measurements within a specified latitude band ($\pm \Psi_{max}$) have no bias while those outside this band have a common bias which is to be estimated.

5.2 Low Earth Orbit

5.2.1 Introduction

The low-earth orbit selected for study was a circular orbit of 915 kilometers (497 nautical miles) altitude and 65 degrees inclination. Performance results were generated using programs SHAD1 and SHAD2 where SHAD1 propagated the covariances along a Keplerian orbit and SHAD2 included the effect of orbital precession due to the earth's zonal harmonic term J_2.

All navigation runs were for a time of flight of ten hours ($\approx$ 5.8 orbits). At the start of each run the uncertainty of each component of satellite position and velocity was usually 1000 meters and 1 meter per

second, respectively, although other values were sometimes used with very little effect on navigation performance after the first orbit of operation. In addition, these uncertainties were initially assumed to be uncorrelated which is seldom the case in real practice and, when included, usually reduces the early transients in the state estimates.

The navigation runs performed with SHAD1 used a time integration step size of 30 seconds. Using the program GTDS in the manner indicated in Section 4.2.3, a value of 2×10^{-15} kilometers/second^2 was obtained for the non-zero terms of the process noise spectral density matrix(Q). For a time step of 30 seconds, the corresponding values of the non-zero terms of the process noise covariance matrix (Q_i) were 6×10^{-14} kilometers^2/second^2.

A typical example of the performance obtained during a navigation run is show in Figure 5-1 where the time histories are given for the standard deviations of the tangential, normal and radial components of satellite position error. The results are for the case where sightings were made on 40 different setting stars per orbit and the stars were restricted to be within 45 degrees of the orbital plane (i.e. the observations were restricted to an azimuth look-angle (ϕ) of 180 ± 45 degrees about the local vertical where zero azimuth is defined to be in the direction of satellite motion). During the early part of the first orbit it is seen in Figure 5-1 that large position error transients occur because of the initial (and uncorrelated) position and velocity uncertainties selected for the navigation run. However, as the navigation filter continues to process measurements, the errors are brought under control during the latter portion of the first orbit and start approaching steady-state levels. Note that at least one of the error components is oscillatory in nature which is actually the case for all three

components and is inherent in the dynamics of this problem. Since these components happen to oscillate asynchronously, it would be ambiguous to quantify the navigator's performance at a specific time such as at the end of the navigation run. A more consistent and representative performance indication is obtained by performing a linear least-squares fit of the data over the last orbital period and extrapolating the resulting line to the final time. For the case in Figure 5-1, the average estimates of the tangential, normal and radial components at the final time are 39, 43 and 11 meters, respectively.

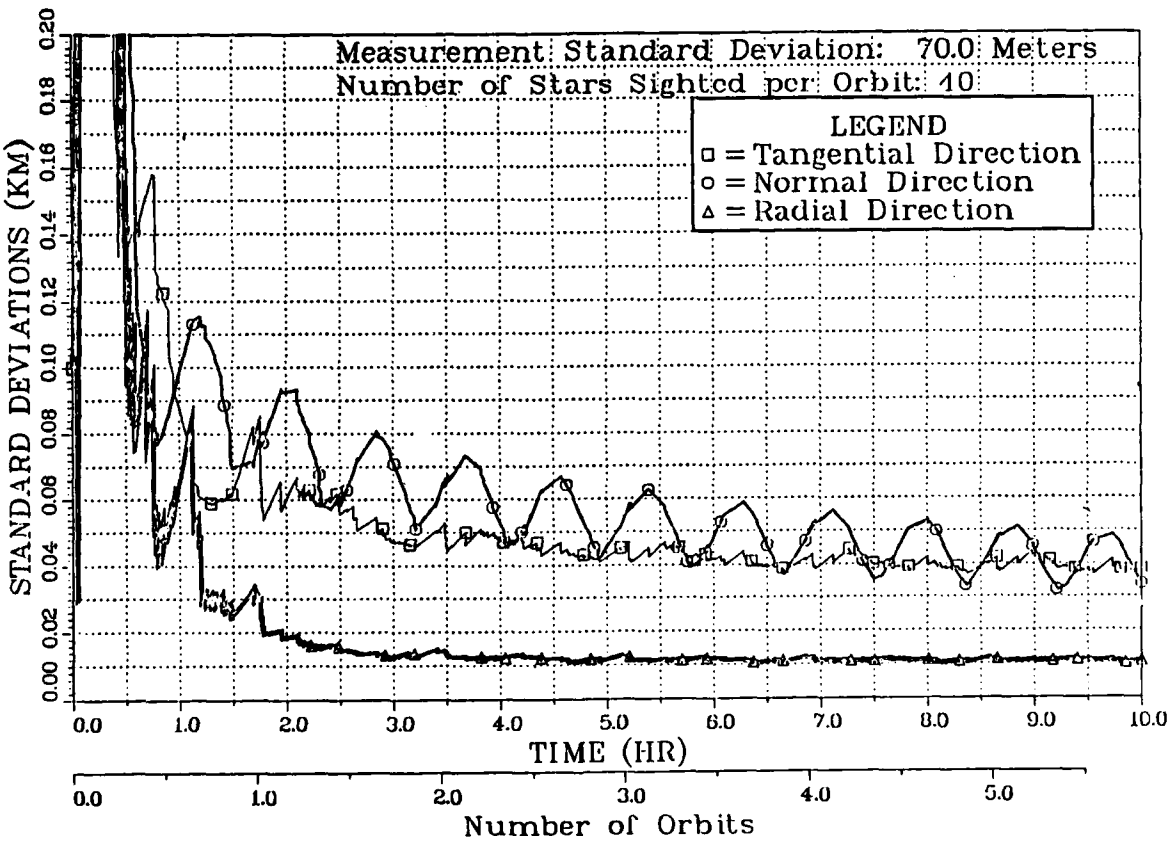

Figure 5-1. Time history of navigation position error standard deviations (low-earth orbit)

5.2.2 SHAD1 Performance Results

5.2.2.1 Bias Option 1 (No Bias)

Before presenting data for those cases containing measurement bias it is felt that some indication should be provided of the performance when there is no bias, and no attempt is made to estimate a bias along with satellite position and velocity. For this option the effect of increasing the number of star sightings per orbit was analyzed for two different sighting-azimuth restrictions.

Figure 5-2 shows the effect of increasing the number of star sightings per orbit when only stars within the azimuth sector of 180 $\pm$ 45 degrees are used. In addition, this figure provides some indication of the effect of restricting the observations to certain latitudinal regions of the world. The data on the left of the vertical dashed line was obtained for observations only within $\pm$ 30° latitude, while that on the right was for observations within $\pm$ 67.5° latitude. Note that most of the performance improvement is achieved after making 30 to 40 star sightings per orbit. Also note that for 30 or more star sightings per orbit there is little to be gained by going from a latitude restriction of $\pm$ 30° to $\pm$ 67.5°. This result tends to support the idea of using only observations within some latitude band about the equator where there is less random and systematic variation in stratospheric density.

Figure 5-3 shows the sensitivity of performance to number of star sightings per orbit when sightings are made in both the 180 $\pm$ 45° and $\pm$ 45° azimuth sectors (i.e. both setting and rising stars are used). It is seen, by comparing Figure 5-3 with Figure 5-2, that little improvement is achieved by including the $\pm$ 45° azimuth sector except for the normal component of position error when the number of star sightings per orbit is small.

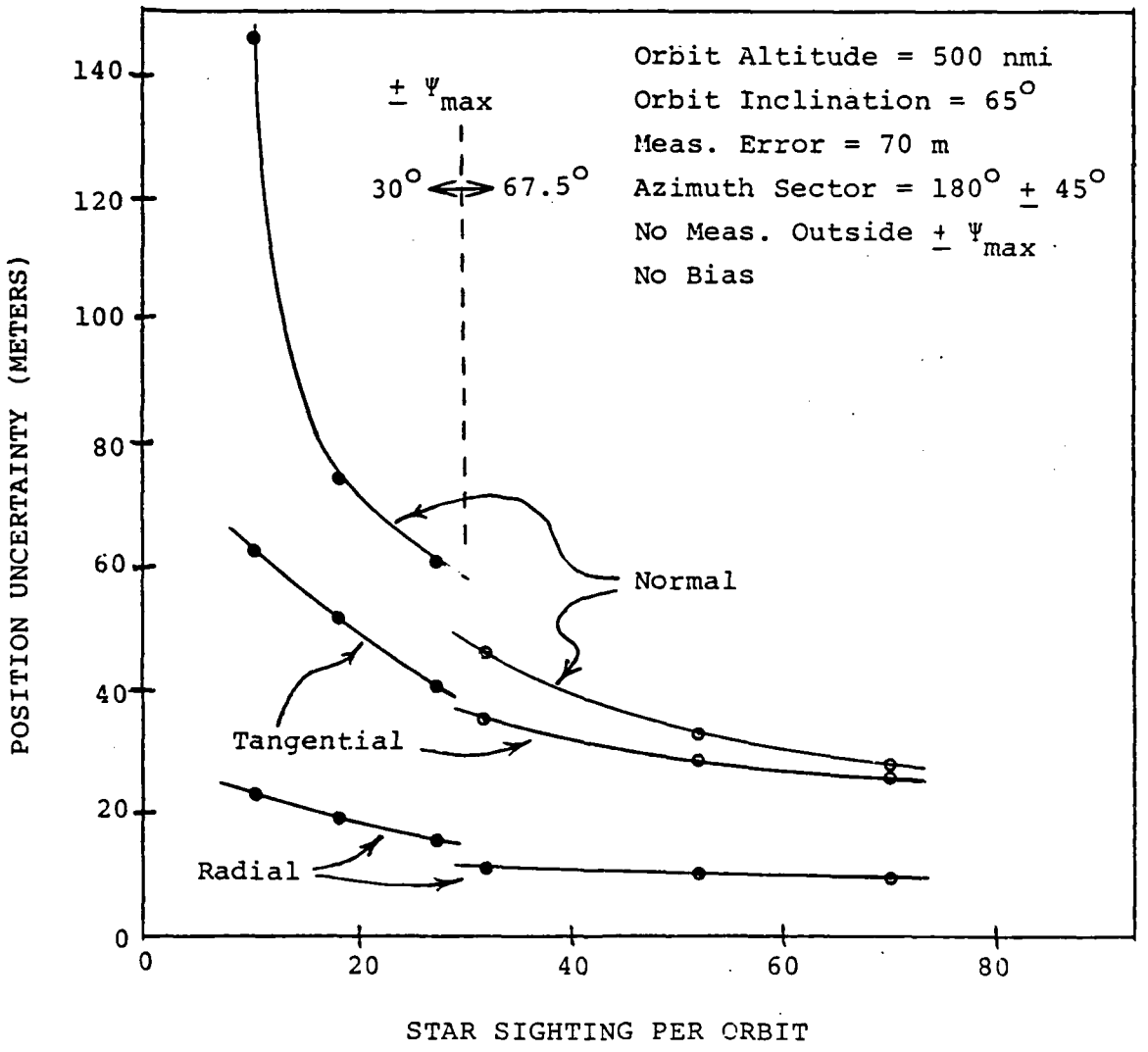

Figure 5-2. Sensitivity of performance to number of star sightings (low-earth orbit).

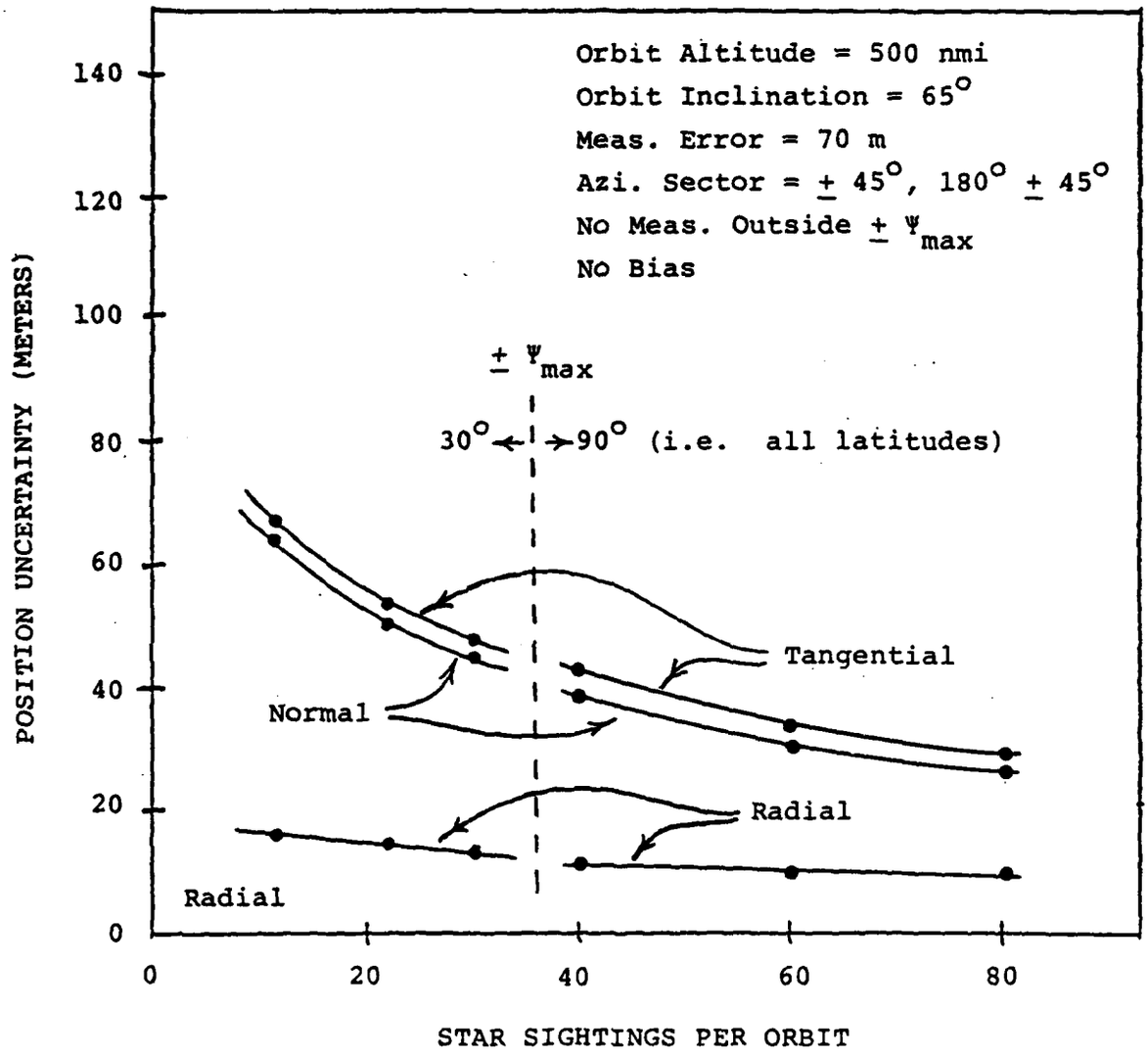

Figure 5-3. Sensitivity of performance to number of star sightings when measurements are made fore and aft (low-earth orbit).

5.2.2.2 Bias Option 2 (Bias Everywhere)

A fixed bias error in all of the observations can be due to one or more of the following:

1) Fixed dispersion/refraction measurement error.

2) Fixed time reference error.

3) Incorrect knowledge of Earth's radius.

4) Fixed atmospheric density error for all observations.

The first two error sources can be minimized by proper system design and the third is considered to be minor. However, the fourth error source is considered to be the most important and likely source because of present limitations in man's knowledge of atmospheric behavior with season, geographic location, etc. Meteorological observations of the stratosphere near the equator indicate a fairly well-behaved and predictable density with little chance of a meaningful bias error. As one departs from the equator by more than 20 or 30 degrees latitude, there are larger systematic changes which have some meaningful uncertainty. For this reason Option 3, presented later, is felt to be more representative of the situation than Option 2. However, as a matter of interest, some performance data was generated for Option 2.

Figure 5-4 shows the results with Option 2 when star sightings are made within the azimuth sector of 180 $\pm$ 45 degrees. There was no latitude restriction on the star sightings. Note that the performance in estimating the normal and radial components is essentially the same as Option 1 (see

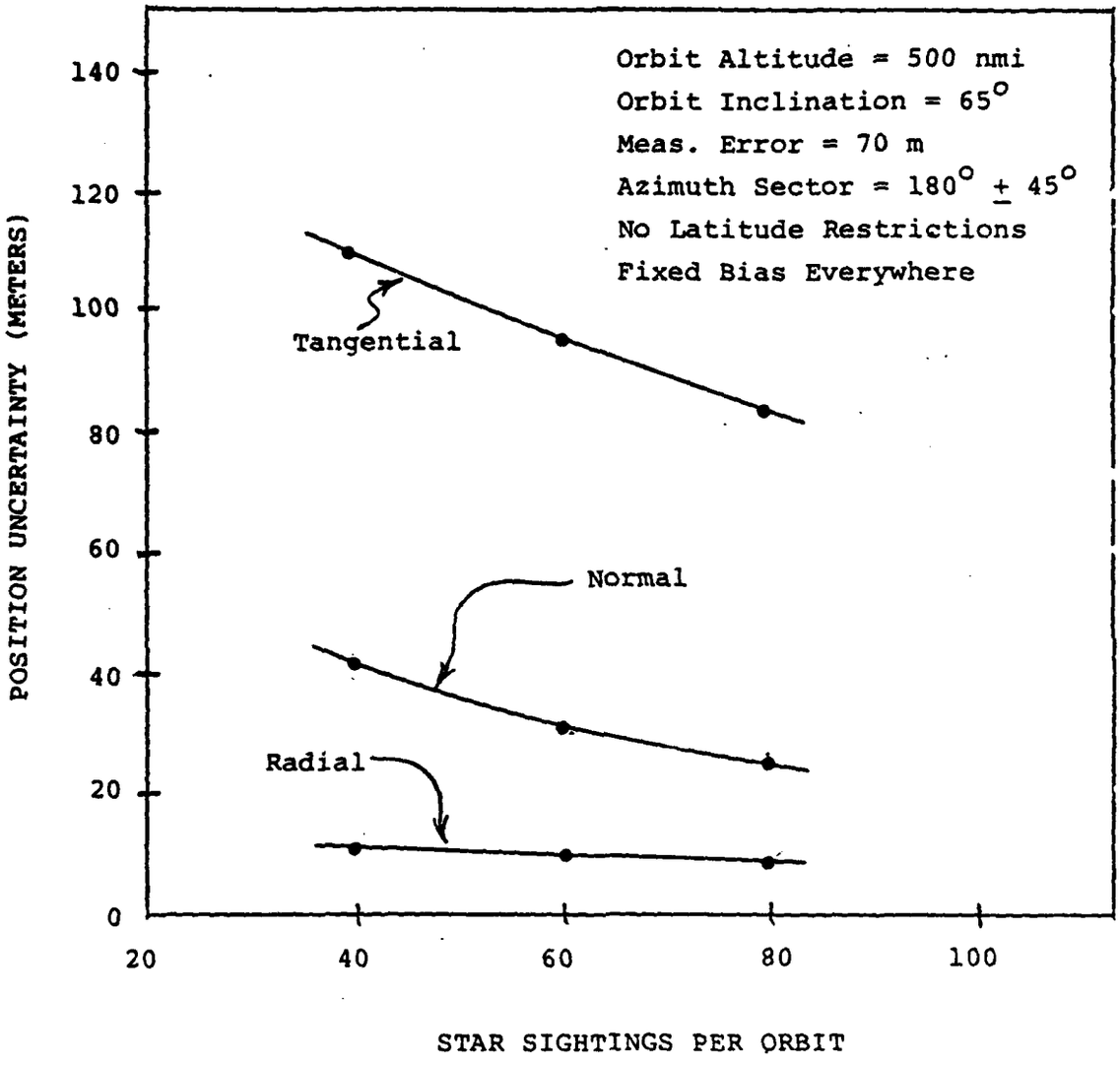

Figure 5-4. Sensitivity of performance to number of star sightings when all measurements are biased (low-earth orbit).

Figure 5-2). However, the tangential position error of 80 to 110 meters is twice as large as that for Option 1. The reason why the tangential performance is not as good is due to the difficulty of the navigation filter in distinguishing between a tangential position error and a measurement bias error when using only star sightings in the aft direction. A larger azimuth sector in the aft direction and/or more orbits of data processing would undoubtedly result in further improvement of the tangential component, however, a more dramatic improvement may be achieved by also using forward star sightings. Use of both forward and aft star sightings enables the navigation filter to easily distinguish between the tangential position error and a measurement bias error. This is clearly demonstrated in Figure 5-5 where star sightings were made in the 180 $\pm$ 45° and $\pm$ 45° azimuth sectors. The overall prerformance is equivalent to that obtained with no measurement bias and demonstrates the ability of the filter to handle a bias.

5.2.2.3 Bias Option 3

Option 3 assumes that all measurements within a specified latitude band ($\pm$ Ψmax) have no bias while those outside have a common bias which is to be estimated. As previously indicated, this option is considered to be the most representative of the three options if the bias is associated with atmospheric density modeling.

Figure 5-6 shows the performance with Option 3 when the azimuth sector is 180 $\pm$ 45° and a bias exist only outside $\pm$ 30° latitude. Note that the performance is similar to that obtained with no bias anywhere (Figure 5-2) even though the star sightings are restricted to the 180 $\pm$ 45° azimuth sector. It would appear that no sightings are required on rising stars (i.e. stars in the forward azimuth sector) if there is no atmospheric bias error within $\pm$ 30° latitude.

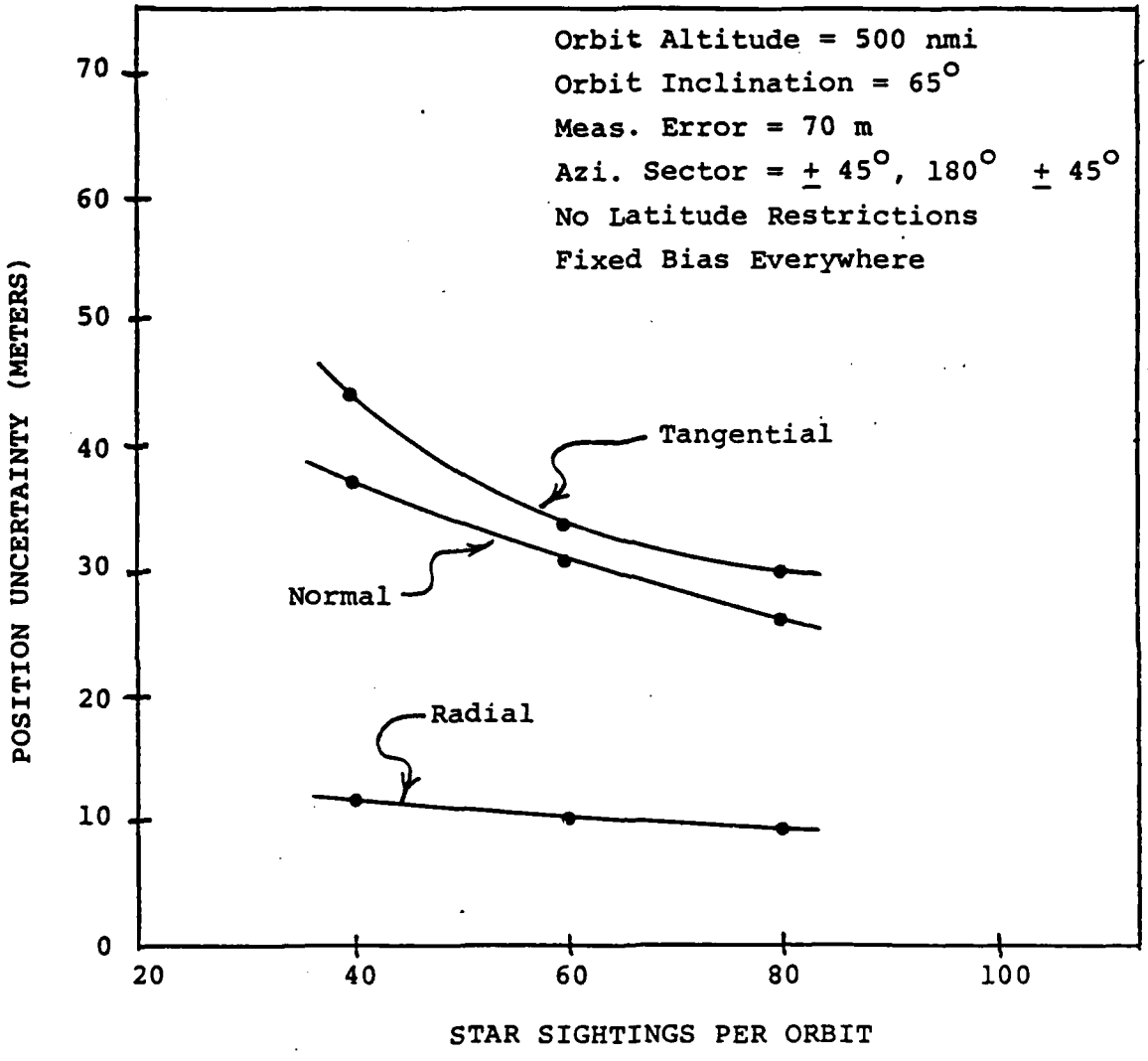

Figure 5-5. Sensitivity of performance to number of star sightings when all measurements are biased but are made fore and aft (low-earth orbit).

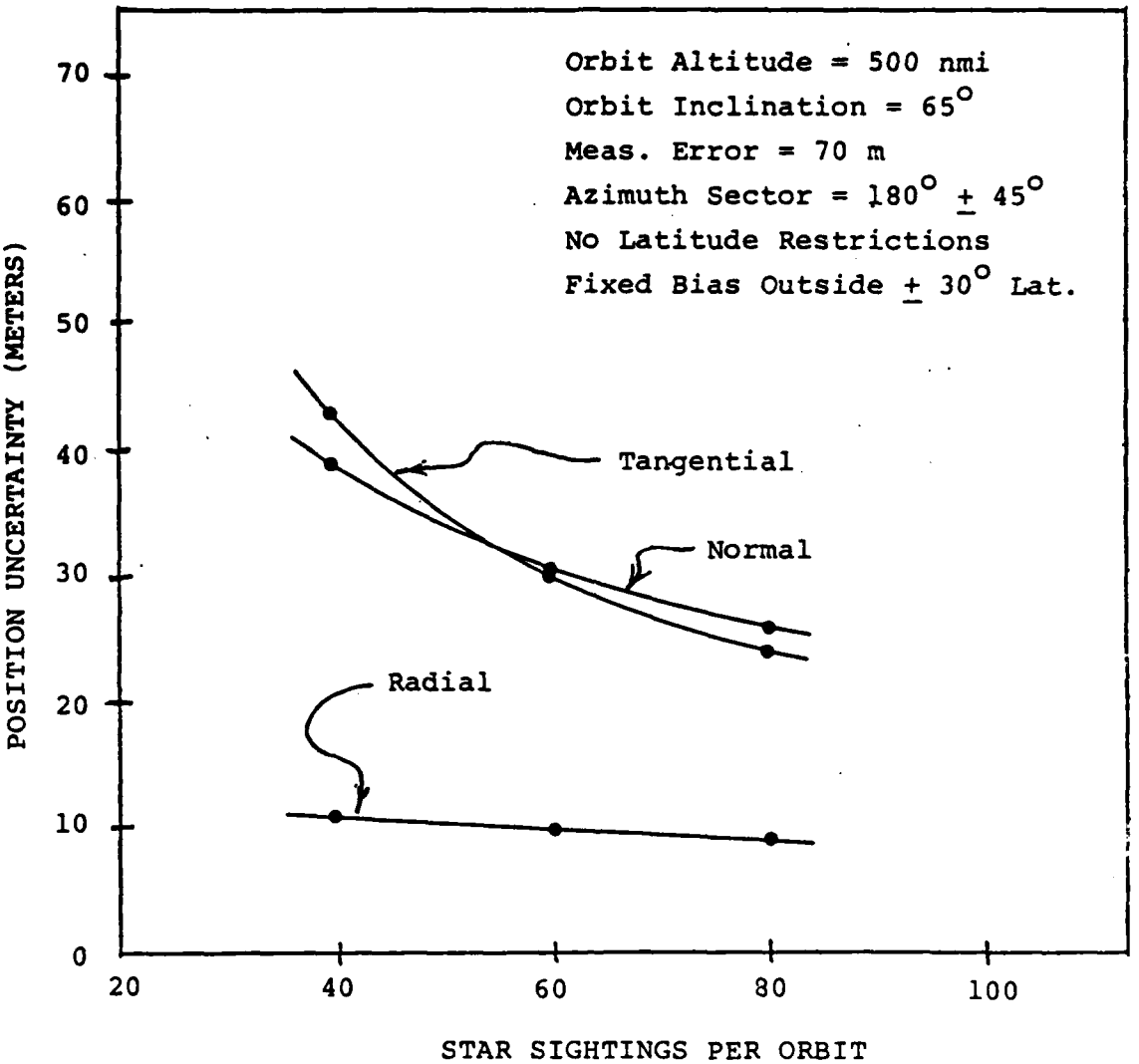

Figure 5-6. Sensitivity of performance to number of star sightings when all measurements outside ± 30° latitude are biased (low-earth orbit).

Shown in Figure 5-7 is the effect of changing the azimuth sector size for star sightings in the aft direction. The results are for 40 star sightings per orbit and no bias within $\pm$ 30° latitude. Note that only the normal component is significantly improved by using a sector size larger than 180 $\pm$ 45 degrees. This is as expected since star sightings at larger azimuth angles with respect to the orbital plane provide more normal positional information. However, it should also be noted that stars at large azimuth angles require more time to enter the atmosphere than those near the orbital plane.

A baseline measurement error of 70 meters (one sigma) was used to generate all of the prior performance data. Figure 5-8 shows the effect of varying this error for the case of 40 star sightings per orbit, no bias within $\pm$ 30° latitude, and an azimuth sector of 180 $\pm$ 45°. It is seen that the effects are fairly linear, with the radial error remaining small and the other two components being about half as large as the measurement error.

5.2.3 SHAD2 Performance Results

The program SHAD2 provides the capability to model satellite orbits more accurately and to base star observations upon real star positions. Since the zonal harmonic coefficient J_2 dominates all other disturbing acceleration coefficients in low-earth orbit, it was decided to study the effect of this term alone on navigation preformance. The star positions were taken from the Yale Bright Star Catalog.

Figure 5-9 shows the effect of varying the number of star sightings per orbit with SHAD2 for the case where the other conditions were the same as those used to generate the SHAD1 results of Figure 5-6 (i.e. star sightings

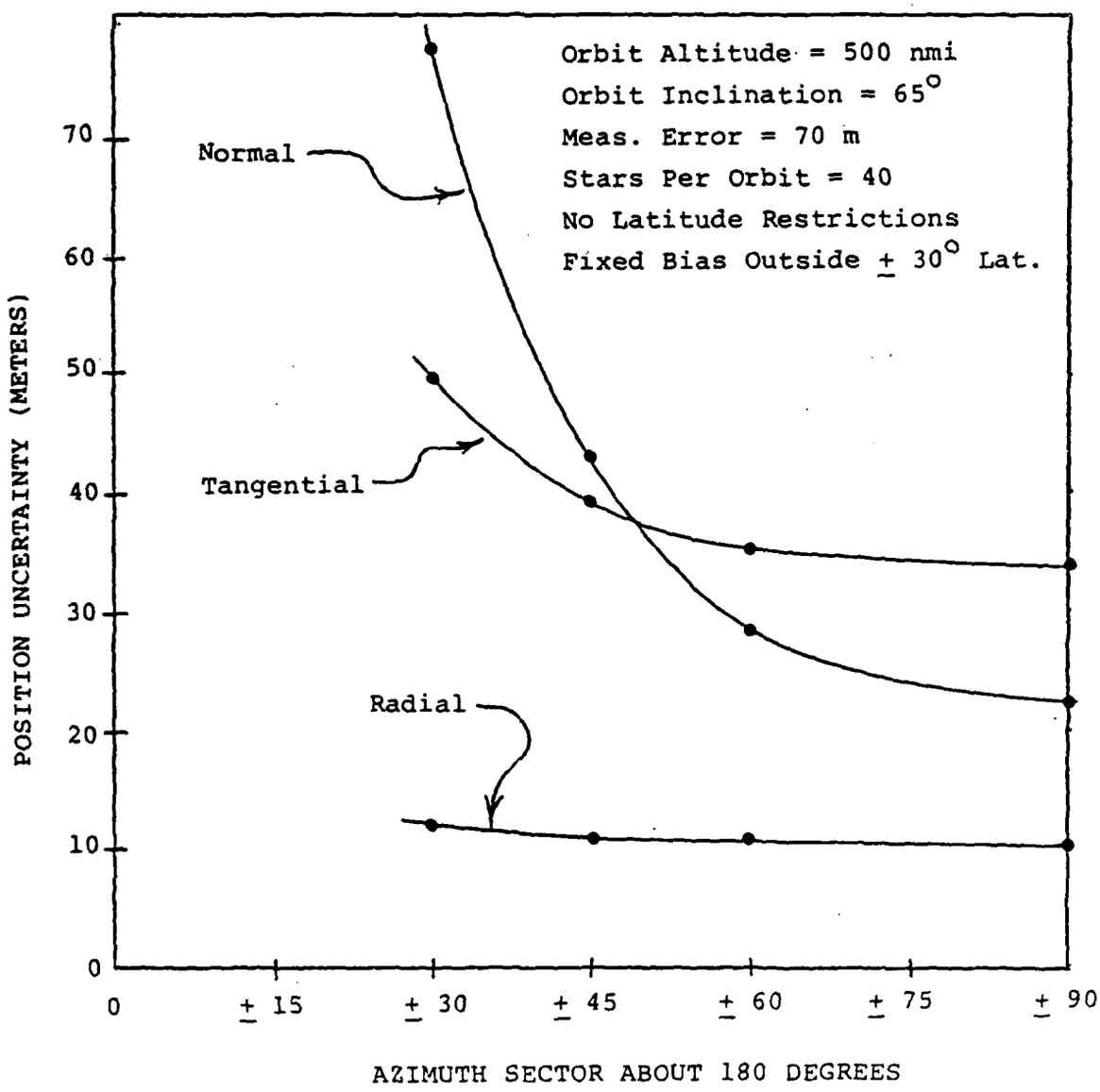

Figure 5-7. Sensitivity of performance to azimuth sector size (low-earth orbit).

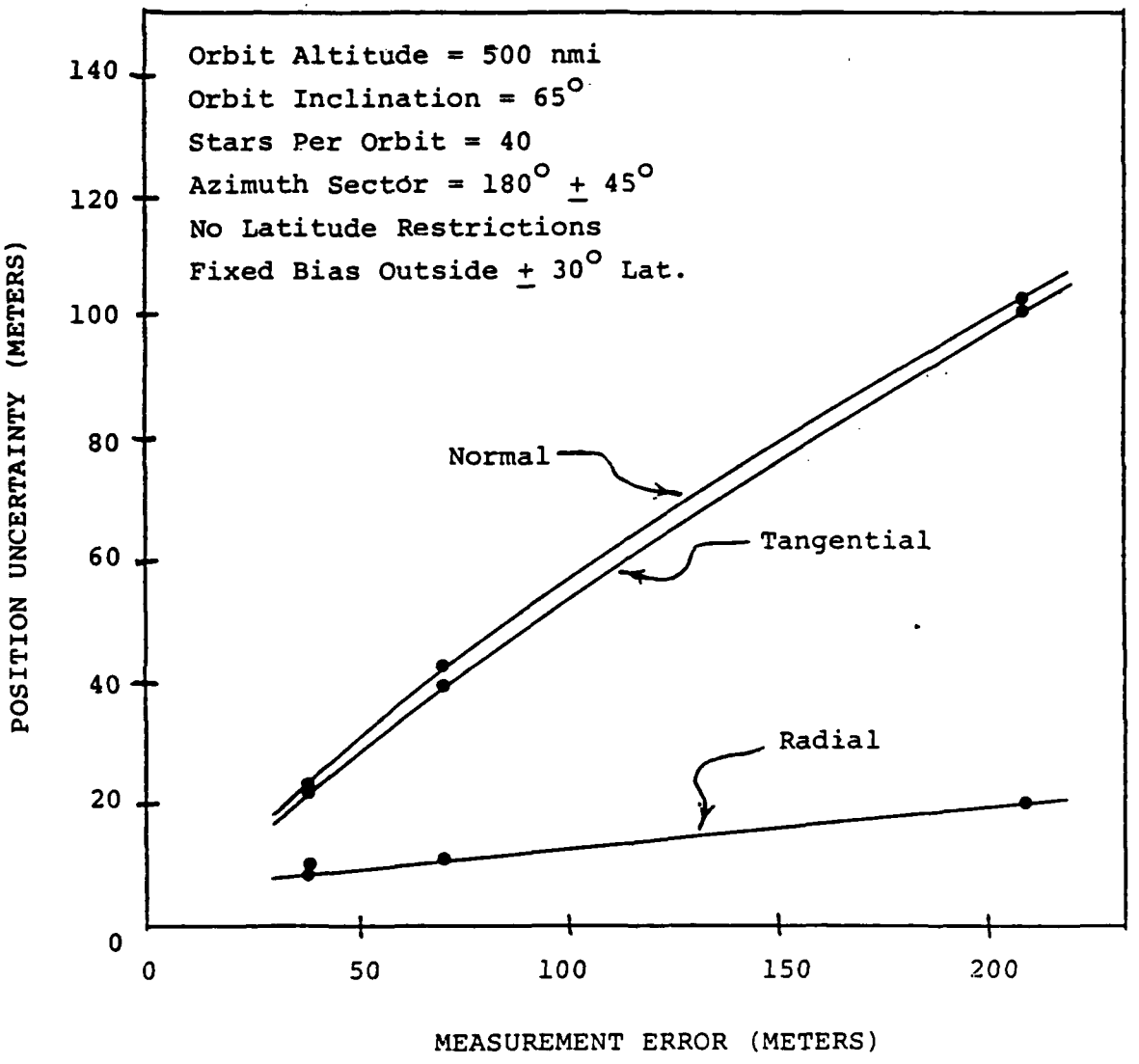

Figure 5-8. Sensitivity of performance to measurement error (low-earth orbit).

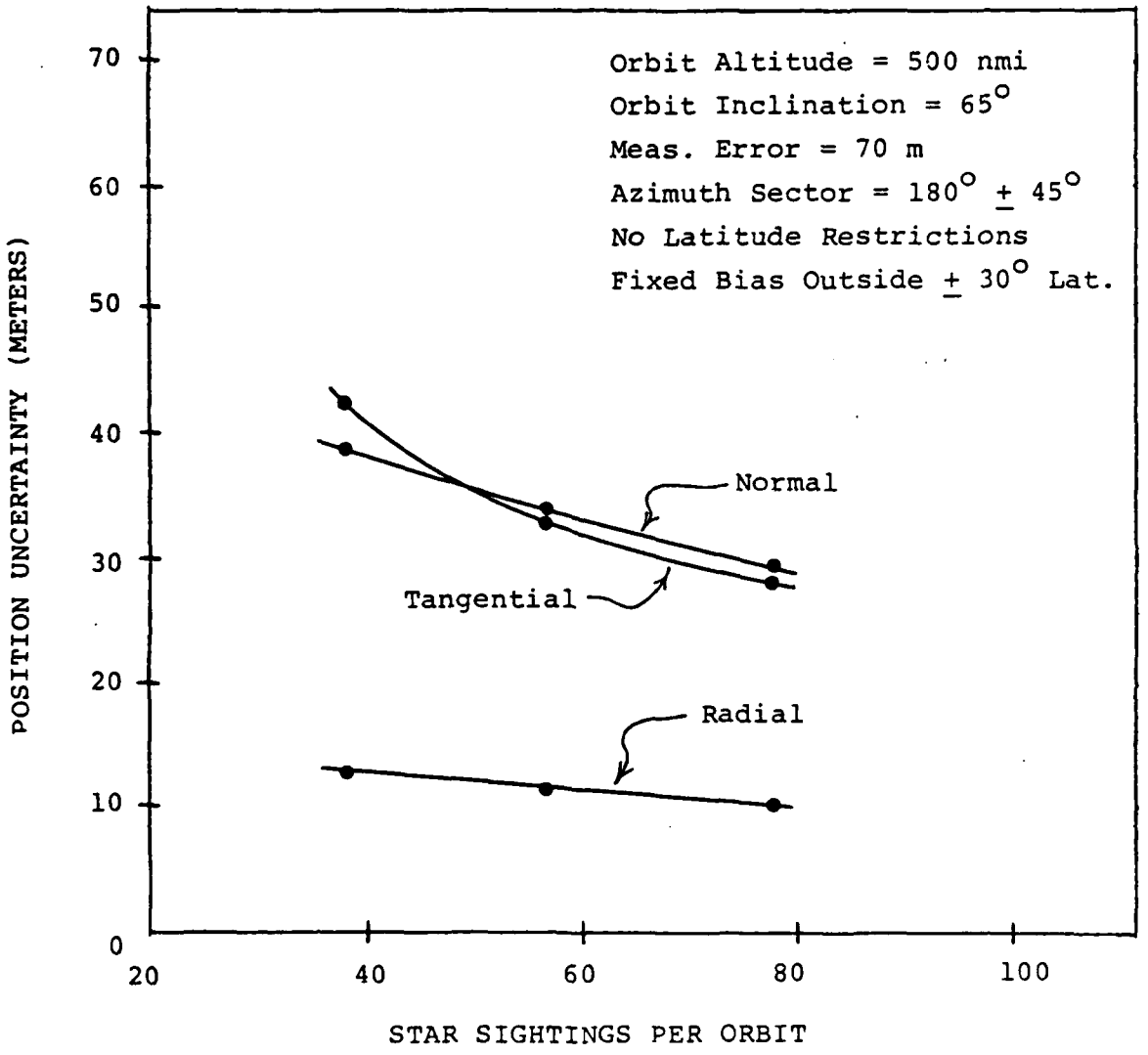

Figure 5-9. Sensitivity of performance to number of star sightings when using SHAD2 program (low-earth orbit).

restricted to an azimuth sector of 180 $\pm$ 45° and a measurement bias only outside $\pm$ 30° latitude). It is seen that the results are about the same as those in Figure 5-6, thus providing some validity to the results of SHAD1. These results were also confirmed by M. Slutsky using the Kalman filtering options of GTDS. As a matter of interest, the left-most set of data points in Figure 5-9 represent the performance near the end of the time history in Figure 5-1.

5.3 GPS Orbit

The second orbit analyzed in the study is similar to that of the Global Positioning System (GPS) and had an altitude of 20,242 km, orbital inclination of 63°, and period of 12 hours.

All of the performance data generated for this orbit was obtained using program SHAD1. The covariance matrix was propagated at 150 second intervals for 100 hours (8.3 orbits). Using the program GTDS in the manner indicated in Section 4.2.3, a value of 1.4×10^{-17} kilometers^2/second^2 was obtained for the non-zero terms of the process noise covariance matrix (Q_i).

A typical example of the performance during a navigation run is shown in the time history of Figure 5-10. The results are for the case of 26 star sightings per orbit with no sightings outside an azimuth sector of 180 $\pm$ 90°, no observations outside $\pm$ 30° latitude and no bias error. It is seen that the initial transients settle out after one orbit of data processing.

Figure 5-11 shows the effect of changing the number of star sightings per orbit when all other conditions remain the same as those of Figure 5-10. The right-most data set of Figure 5-11 represents the final average values of the time histories in Figure 5-10.

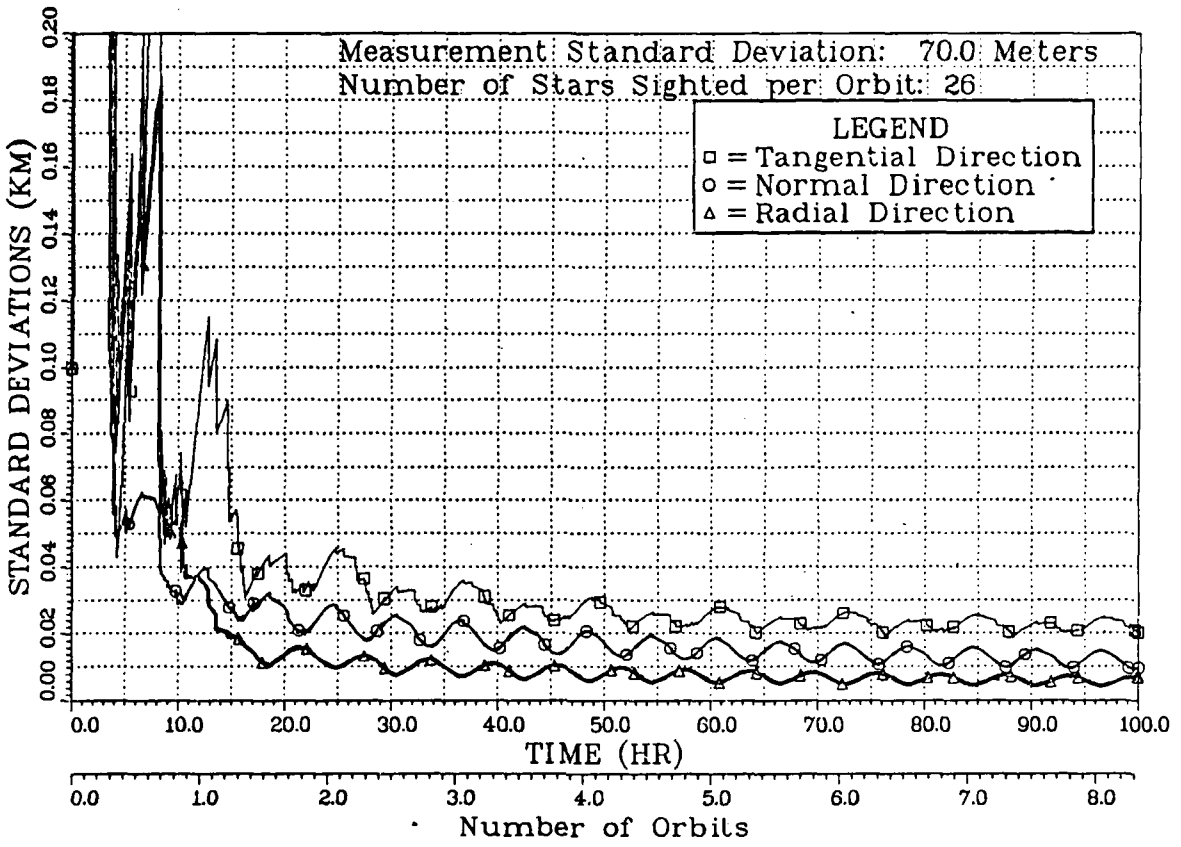

Figure 5-10. Time history of navigator position error standard deviations (GPS orbit).

Figure 5-12 shows the effect of changing the number of star sightings per orbit when all other conditions are the same as those of Figure 5-11 except that observations are also permitted outside $\pm$ 30° latitude but contain a bias error which is to be estimated. No latitude restrictions permit observations to be made throughout the orbit, however, it is seen that, for 20 or more star sightings per orbit, the performance is only slightly better than that of Figure 5-11 where all of the observations were inside $\pm$ 30° latitude.

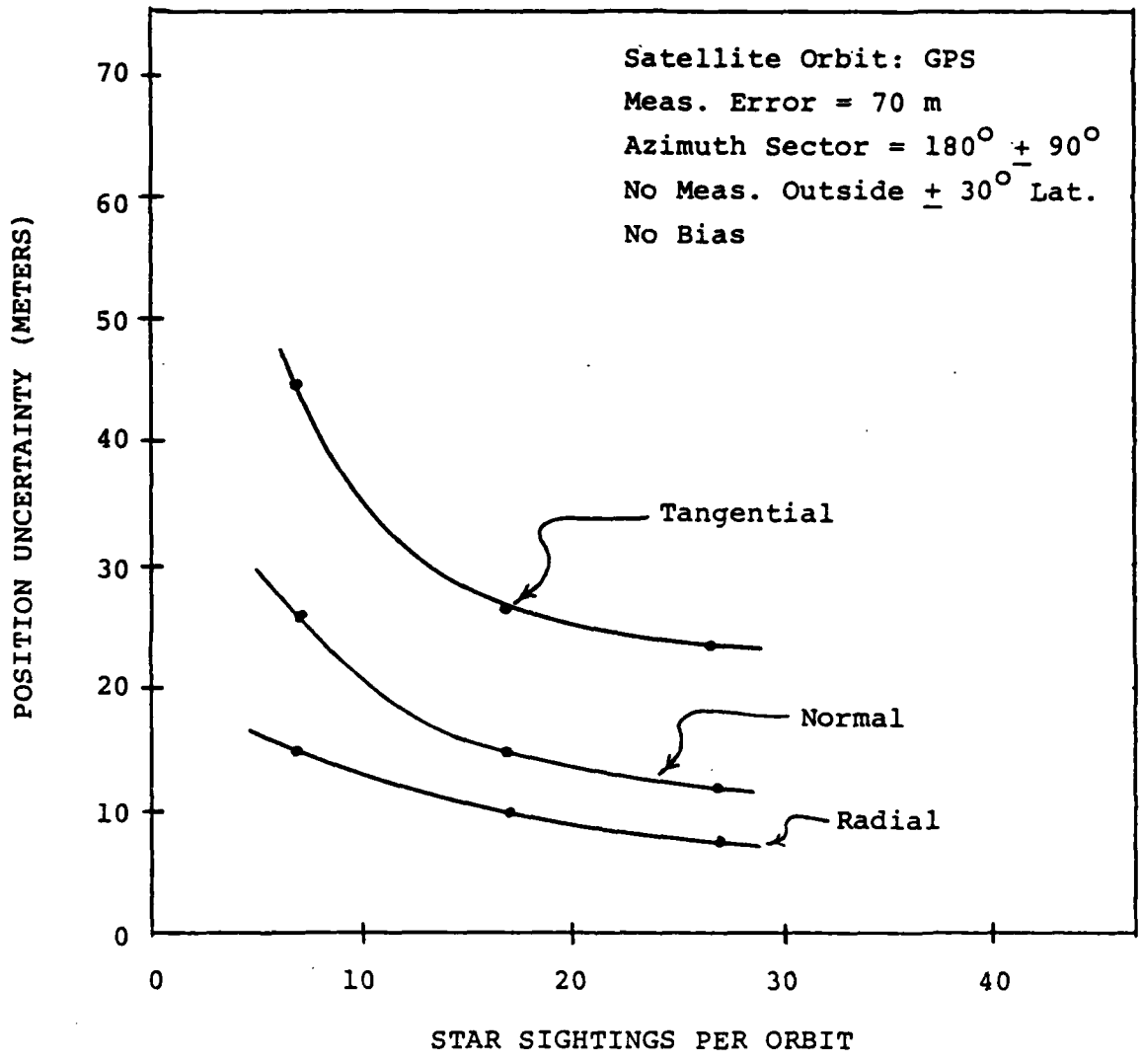

Figure 5-11. Sensitivity of performance to number of sightings when all measurements are within ± 30° latitude (GPS orbit).

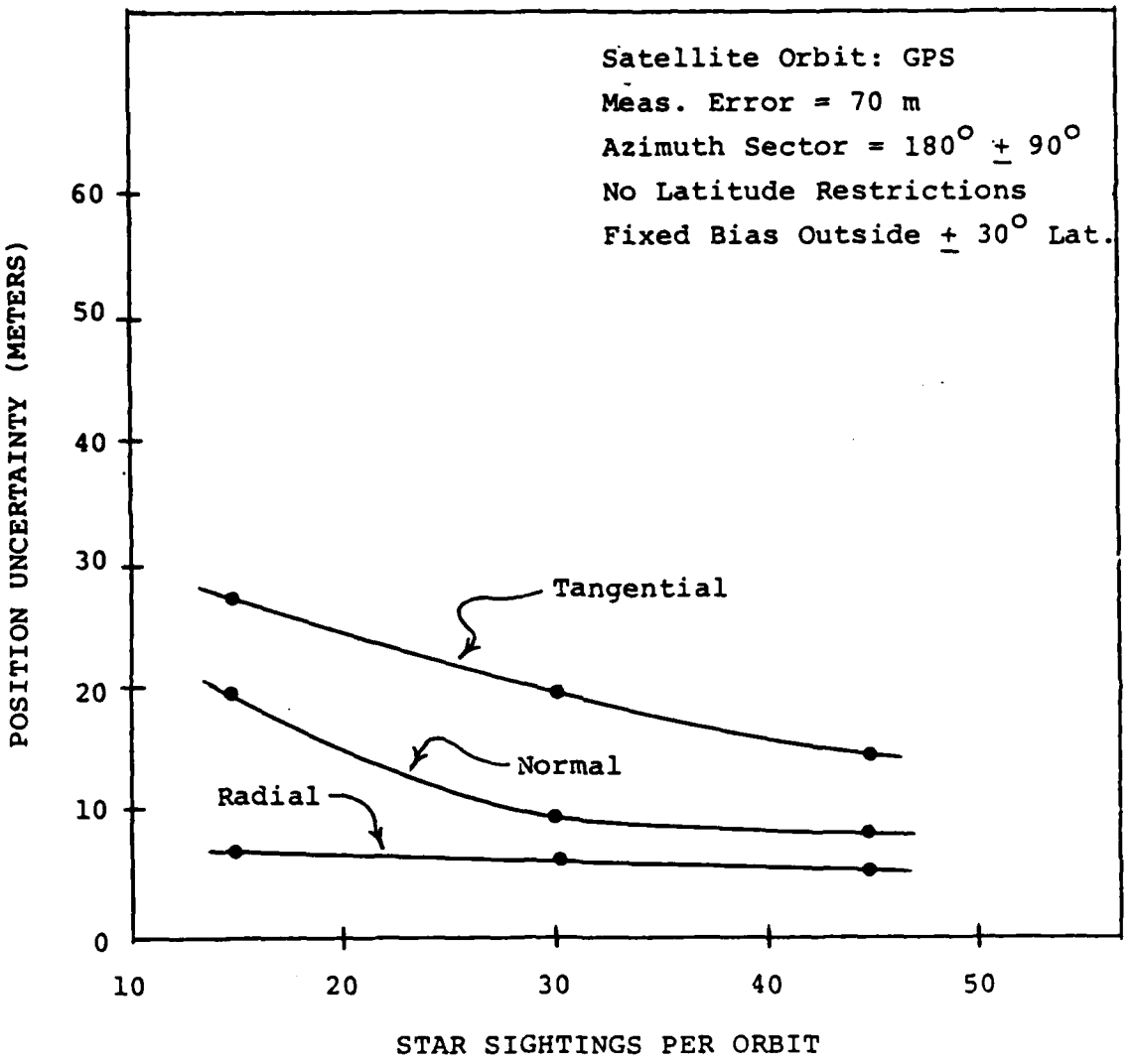

Figure 5-12. Sensitivity of performance to number of sightings when all measurements outside ± 30° latitude have a bias (GPS orbit).

The sensitivity of performance to measurement error is shown in Figure 5-13 for the case of 10 star sightings per orbit and for an azimuth sector of 180° ± 45°. Note that the normal component of position uncertainty is now larger than the tangential component primarily because the azimuth sector is smaller than that used for the results in Figures 5-11 and 5-12.

5.4 Geosynchronous Orbit

The third orbit analyzed in the study was a geosynchronous orbit which lies within the equatorial plane and has an altitude of 35,866 km and orbital period of 24 hours.

All of the performance data generated for this orbit was obtained with the SHAD1 program. The covariance matrix was propagated at 300 second intervals for 200 hours. Using the program GTDS in the manner indicated in Section 4.2.3, a value of 1.5×10^{-20} kilometers^2/second^2 was obtained for the non-zero terms of the process noise covariance matrix (Q_i).

All of the performance results presented for the geosynchronous orbit are for Bias Option 3 (see Section 5.2.2.3) where all observations within a specified latitude band (± 30°) have no bias while those outside have a common bias which is to be estimated.

Figure 5-14 shows the navigator performance as a function of the number of star sightings per orbit. Since the satellite velocity is much slower than at low-earth orbit, the amount of divergence in the error covariance matrix between measurements is also much slower. Thus, the reduced number of grazing stars seen from this altitude does not sacrifice performance compared to low-earth orbit.

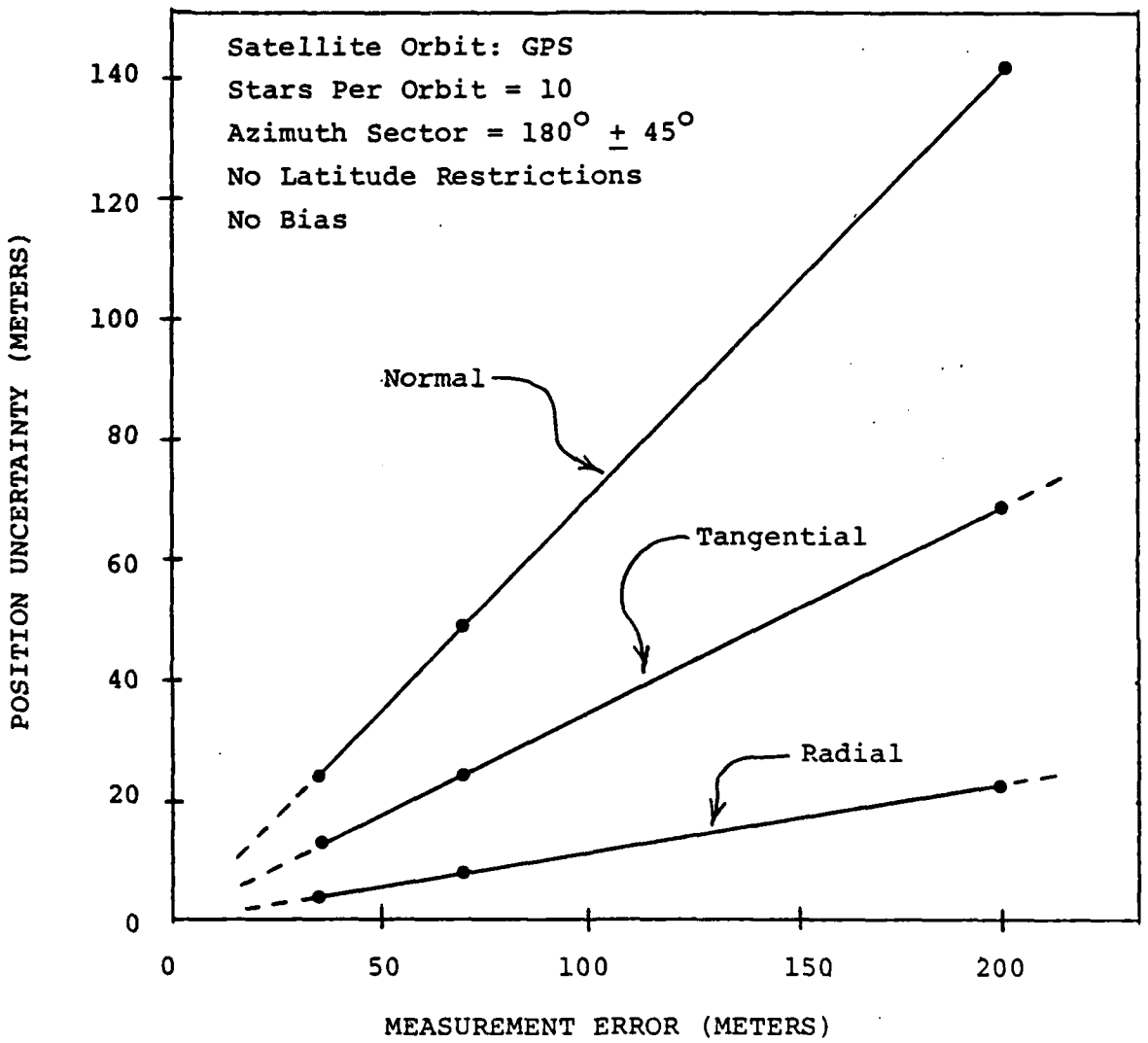

Figure 5-13. Sensitivity of performance to measurement error (GPS orbit).

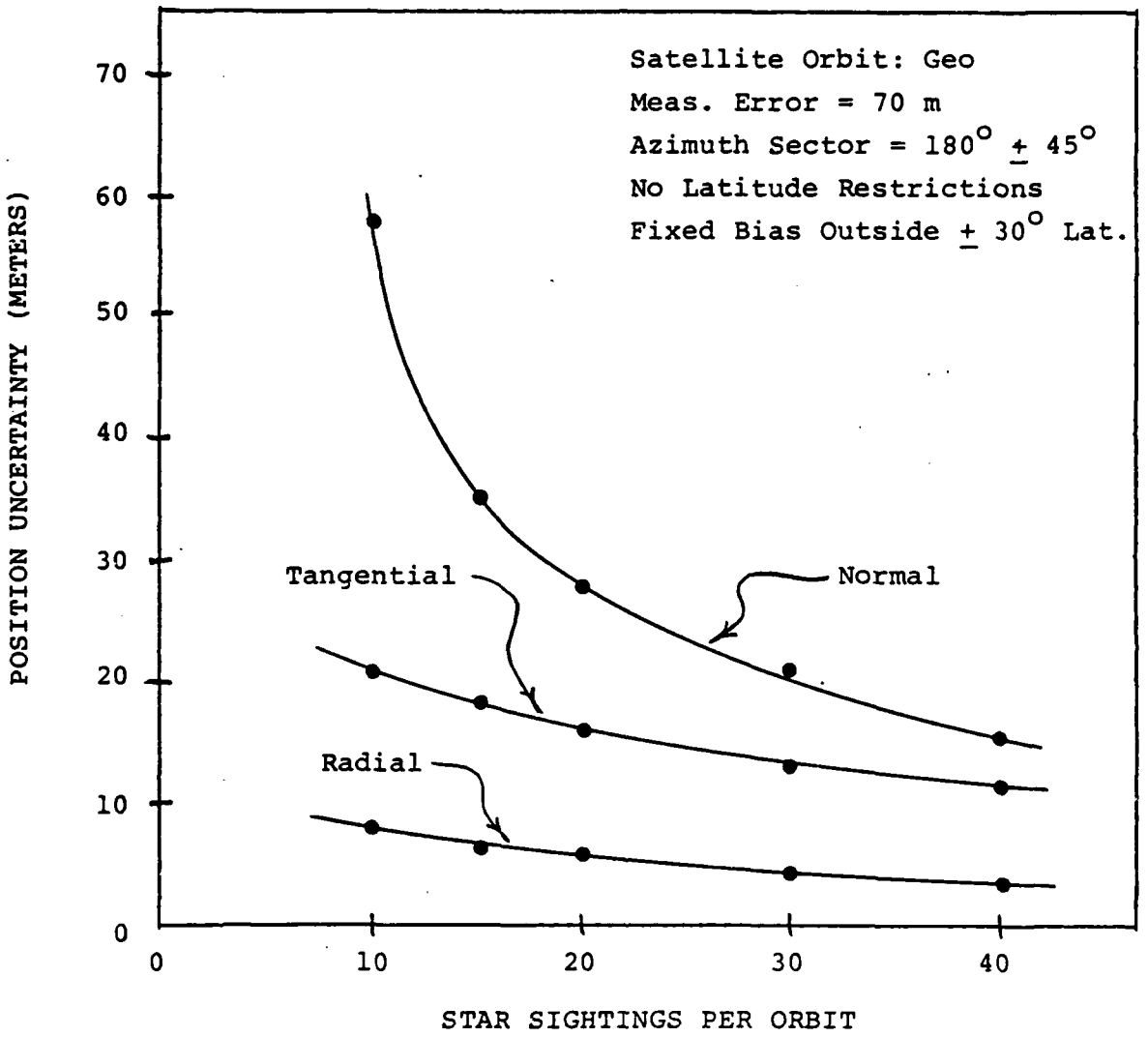

Figure 5-14. Sensitivity of performance to number of star sightings (geosynchronous orbit).

The sensitivity of performance to measurement error is shown in Figure 5-15 for the case of 10 star sightings per orbit. Here again, it is seen that the sensitivities are similar to those obtained for the GPS orbit, with the normal component of position uncertainty being about twice as large as the tangential component.

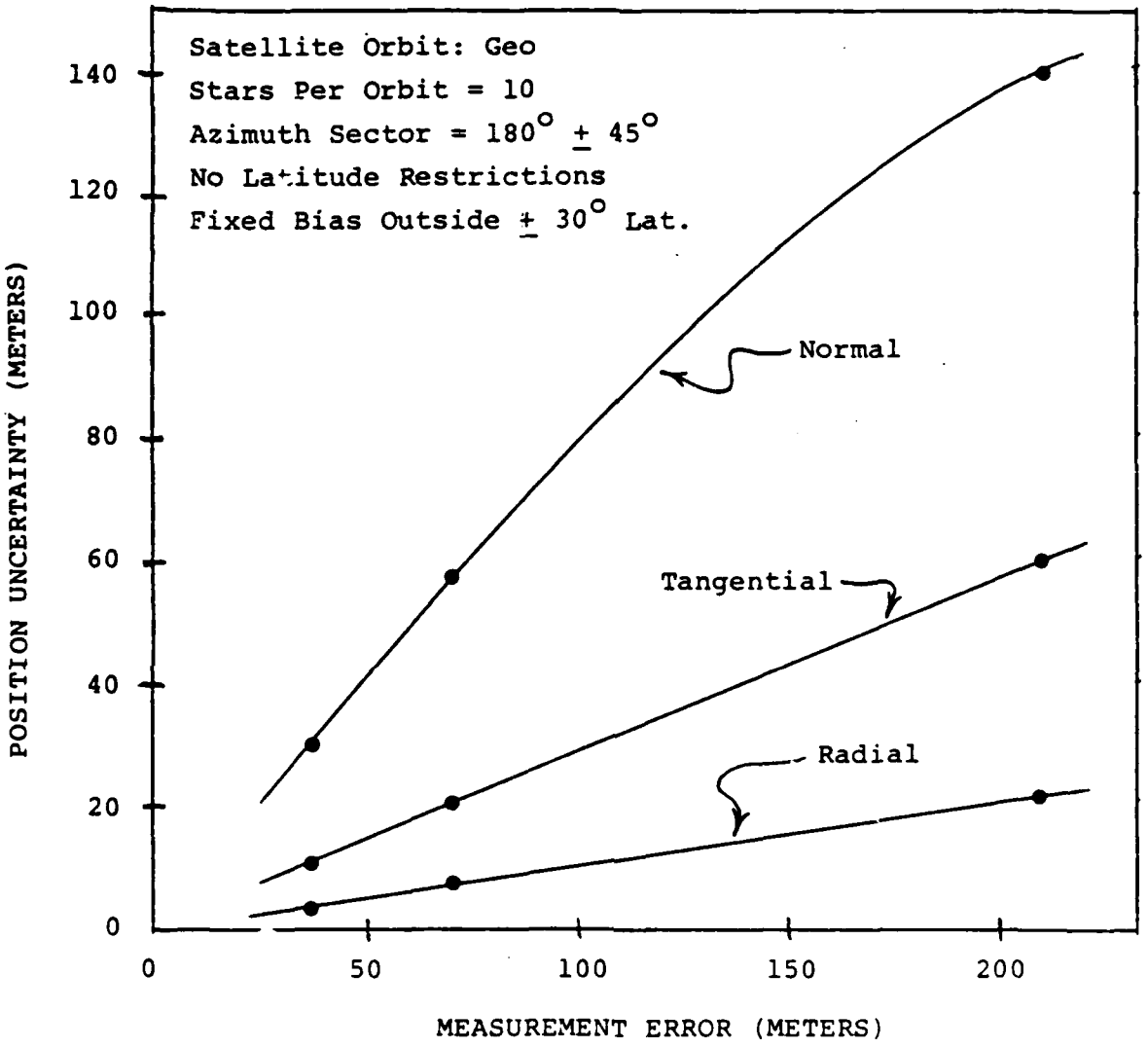

Figure 5-15. Sensitivity of performance to measurement error (geosynchronous orbit).

APPENDIX A

Derivation of $h_a(R, \rho_o)$ for an Exponential Atmosphere

The density of an exponential atmosphere is completely defined by the following:

$$\rho = \rho_o \exp\left[-\frac{h - h_o}{H}\right] \tag{A-1}$$

where ρ is the density at altitude h, ρ_o is the density specified at some arbitrary altitude h_o, and H is the specified constant for density scale height. According to Equation 2-6 the approximate refraction for this atmosphere is as follows:

$$R = k(\lambda)\rho_g\left[\frac{2\pi\,(r_e + h_g)}{H}\right]^{\frac{1}{2}} \tag{A-2}$$

where h_g is the grazing height of the refracted ray and ρ_g is the density at that height. Since $r_e >> h_g$ the refraction may be expressed as follows:

$$R = k(\lambda)\rho_g\left[\frac{2\pi\, r_e}{H}\right]^{\frac{1}{2}} \tag{A-3}$$

Using Equation A-1 the density ρ_g can be expressed as

$$\rho_g = \rho_o \exp\left[-\frac{h_g - h_o}{H}\right] \tag{A-4}$$

which when substituted for ρ_g in Equation A-3 yields

$$R = k(\lambda)\rho_o\left[\frac{2\pi\ r_e}{H}\right]^{\frac{1}{2}}\ \exp\left[-\frac{h_g - h_o}{H}\right] \qquad \text{(A-5)}$$

Inverting the above expression gives

$$h_g = h_o - H\ \ln(R) + H\ \ln\left[k(\lambda)\rho_o\left[\frac{2\pi\ r_e}{H}\right]^{\frac{1}{2}}\right] \qquad \text{(A-6)}$$

According to Equation 2-18 the relationship between the apparent height (h_a) and grazing height (h_g) for a spherically stratified atmosphere is

$$h_a = \left[1 + k(\lambda)\ \rho_g\right] h_g + k(\lambda)\rho_g\ r_e \qquad \text{(A-7)}$$

Since the term $k(\lambda)\rho_g$ is never any larger than about 2×10^{-5} for altitudes above 20 kilometers, it may be neglected in the first expression on the right of Equation A-7 so that

$$h_a \approx h_g + k(\lambda)\rho_g\ r_e \qquad \text{(A-8)}$$

Substituting for ρ_g from Equation A-3 and for h_g from Equation A-6 gives

$$h_a(R, \rho) = h_o - H\ \ln(R) + H\ \ln\left[k(\lambda)\rho_o\left[\frac{2\pi\ r_e}{H}\right]^{\frac{1}{2}}\right] + R\left[\frac{H\ r_e}{2\pi}\right]^{\frac{1}{2}} \qquad \text{(A-9)}$$

LIST OF REFERENCES

1. Paulson, D.C., "Autonomous Satellite Navigation From Strapdown Landmark Measurements," Proc. 3rd Symp. on Nonlinear Estimation Theory (San Diego, CA, September 1972), p. 167-182.

2. Lowrie, J.W., "Autonomous Navigation Systems Technology Assessment," AIAA Report No. 79-0056, January 1979.

3. Fang, B.T., "Satellite-To-Satellite Tracking Orbit Determination," Journal of Guidance and Control, Vol. 2, No. 1, Jan.-Feb. 1979, p. 57-64.

4. Marshall, M.H., "Goals for Air Force Autonomous Spacecraft," Jet Propulsion Laboratory, Report No. SD-TR-81-72, 1981.

5. Pease, G.E., and H.T. Hendrickson, "Autonomous Navigation Accuracy Using Simulated Horizon Sensor and Sun Sensor Observations," Aerospace Corporation, Los Angeles, CA, (Available NTIS SAP:HC A20/MF A01), October 1980.

6. Hoag, D.G., "The History of Apollo On-Board Guidance, Navigation, and Control," (presented at the International Space Hall of Fame Dedication Conference, October 1976), The Charles Stark Draper Laboratory, Inc., Cambridge, MA, Report No. CSDL-P-357, 1976.

7. Lillestrand, R.L., and J.E. Carroll, "Horizon-Based Satellite Navigation Systems," IEEE Transaction on Aerospace and Navigational Electronics, September 1963, p. 247-270.

8. Barnes, F., "Earth Horizon Sensing by Stellar Refraction Measurement," The Charles Stark Draper Laboratory, Inc., Cambridge, MA, Intralab Memorandum No. AGS-25-75, 16 October 1975.

9. Elden, B., "The Dispersion of Standard Air," Journal of Optical Society of America, Vo. 43, No. 5, May 1953, p. 339-344.

10. U.S. Standard Atmosphere, 1976, NOAA - S/T 76-1562, NOAA, NASA, U.S. Air Force, Washington, D.C., October 1976.

11. Barnes, F., "Starlight Refraction by Ray-Tracing thru Modeled Earth Atmospheres Using the "RFRAC3," Program, "The Charles Stark Draper Laboratory, Inc., Cambridge, MA. Intralab Memorandum No. AGS-19-81, 2 November 1981.

12. Cole, A.E., and A.J. Kantor, "Air Force Reference Atmospheres," Air Force Geophysics Laboratory, Hanscom AFB, MA, Report No. AFGL-TR-78-0051, 28 February 1978.

13. Cole, A.E., A.J. Kantor, and C.R. Philbrick, "Kwajalein Reference Atmospheres, 1978," Air Force Geophysics Laboratory, Hanscom AFB, MA, Report No. AFGL-TR-79-0241, 24 September 1978.

14. Gelb, A., (ed.), "Applied Optimal Estimation," MIT Press; Cambridge, MA, 1974.

15. Goodyear, W.H., "Completely General Closed-Form Solution for Coordinates and Partial Derivatives of the Two-Body Problem," Astronomical Journal, Vol. 70, No. 3, April 1965, pp. 189-192,

16. Gai, E., and R.C. Hutchinson, "On-Board Navigation Equations," The Charles Stark Draper Laboratory, Inc., Cambridge, MA, Report No. CSDL-C-5360, November 1980.

17. Schweppe, F.C., "Uncertain Dynamic Systems," Prentice-Hall, Englewood Cliffs, New Jersey, 1973.

18. Computer Sciences Corporation and Systems Development and Analysis Branch (GSFC), joint ed., "Goddard Trajectory Determination System: User's Guide, " July 1978.

19. Battin, R.H., "Astronomical Guidance," McGraw-Hill, New York, NY, 1964.